PHYSICAL REVIEW FLUIDS **9**, 043905 (2024)

Transient energy growth in channel flow with compliant walls

Frédéric Alizard, Benoît Pier, and Smail Lebbal
Laboratoire de mécanique des fluides et d'acoustique, CNRS, École centrale de Lyon, Université de Lyon 1, INSA Lyon, 36 avenue Guy-de-Collongue, 69134 Écully, France

(Received 14 September 2023; accepted 19 March 2024; published 9 April 2024)

In this paper, we present a Lagrangian method for searching initial disturbances which maximize their total energy growth after a certain time horizon for linearized fluid-structure interaction problems. We illustrate this approach for the channel flow case with compliant walls. The walls are represented as thin spring-backed plates, the so-called Kramer-type walls. For nearly critical values of the control parameters (reduced velocity V_R and Reynolds number Re), analyses for sinuous or varicose perturbations show that the fluid-structure system can sustain two types of oscillatory motions of large amplitude. The first motion is associated with two-dimensional perturbations that are invariant in the spanwise direction. For that case and a certain range of streamwise wavenumbers, the short-time dynamics of sinuous perturbations is driven by the nonmodal interaction between the Tollmien-Schlichting and the traveling-wave flutter (TWF) modes. The amplitude of the oscillation is found to increase with the reduced velocity, and the optimal gain exhibits larger values than its counterpart computed for a channel flow between rigid walls. For perturbations of varicose symmetry, the transient energy is rapidly governed by the unstable TWF mode without a clear low-frequency oscillation. The second type of motion concerns streamwise-invariant and spanwise-periodic perturbations. In that situation, it is found that perturbations of sinuous symmetry exhibit the largest amplification factors. For moderate values of the reduced velocity, $V_R = \mathcal{O}(1)$, the dynamics is the result of a simple superposition of a standing wave, due to traveling-wave flutter modes propagating downstream and upstream, and the roll-streak dynamics. The variations of these oscillations with the reduced velocity, spanwise wavenumber, and Reynolds number are then investigated in detail for the sinuous case.

DOI: 10.1103/PhysRevFluids.9.043905

I. INTRODUCTION

The interaction between fluid flow and compliant walls has a wide variety of applications in both biological and engineering systems. For instance, after the seminal experiments of Kramer [1], many researchers have illustrated the performance of compliant coatings by altering the flow favorably to extend the laminar region (see Ref. [2] and the recent work of Nagy *et al.* [3]). In the biological context, wall deformability plays an important role in blood flow as well as peristaltic transport, for example, through the intestines and the urogenital tract (see Refs. [4,5] for a review).

In that respect, many efforts have been made to design a representative compliant wall model and to study the asymptotic linear stability due to the coupling between the fluid flow and the solid structure (see the recent review of Kumaran [6]). Among them, the surface-based model consisting of an infinitely thin plate mounted on springs and dampers (the so-called Kramer wall) which interacts with a shear flow received considerable attention over the last few decades. Carpenter and Garrad [7,8] focused on the stability of boundary-layer flows over Kramer-type compliant walls. They provided some confirmation of the transition-delaying potential of compliant coatings. For this model, Carpenter and Garrad [7,8] identified two categories of instability modes: the fluid-based Tollmien-Schlichting (TS) mode and solid-based fluid-structure instabilities, referenced as FSI modes hereafter. The last category includes both the traveling-wave flutter (TWF) modes and the (almost static) divergence (DIV) modes.

The mechanism responsible for the growth of TWF modes is similar to that governing water surface waves generated by wind [9,10]. The DIV mode is either interpreted as an absolute instability [11] or a modal instability with a nearly vanishing phase velocity for high values of the wall dissipation [12].

While a wide number of investigations has been devoted to study the long-time regime of these instabilities [13–16], only a few have focused on the short-time dynamics. Among them, Hœpffner *et al.* [17] studied the transient energy growth mechanisms for perturbations developing in a channel flow with Kramer-type compliant walls. Their analysis was restricted to streamwise-invariant perturbations (i.e., varying the spanwise wavenumbers β at fixed streamwise wavenumber $\alpha = 0$). The solution is obtained by summing over the eigenmodes that collectively exhibit nonmodal growth. The authors have shown that, for large wall elasticity, the flow can sustain standing waves with large oscillations in time. The most amplified perturbations exhibit sinuous symmetry and are well described by an added-mass effect. The flow behavior is then essentially driven by the standing-wave dynamics rather than by the lift-up effect. However, the authors failed to obtain convergence when increasing the number of modes used in the summation. Thus, a complete overview of the wall flexibility effects onto transient energy growth is still missing. More specifically, the significant case where streaks interact with the standing wave for moderate wall flexibility has not been explored by the previous authors.

For the same flow case, Zengl and Rist [18] computed the optimal gain map in the streamwise-spanwise wavenumber plane with a similar numerical method. These authors showed that the optimal gain does not significantly depend on the wall flexibility. They have also observed that the flow can sustain strong oscillations for oblique waves due to wall compliance. However, the underlying mechanisms are not fully discussed in that study. In addition, this analysis has been carried out for only a single set of compliant wall parameters.

More recently, for pulsatile plane Poiseuille flow bounded by compliant walls, Tsigklifis and Lucey [19] investigated mainly the intracyclic growth features, i.e., the modulation amplitude of a given Floquet mode. Nevertheless, a complete study of nonmodal growth mechanisms associated with the steady case is not given by these authors.

While the analyses discussed above have provided significant insight into some nonmodal mechanisms of a flow interacting with compliant boundaries, they only focus on specific parameter ranges and do not fully capture the complete transient growth scenarios due to the entire set of eigenmodes. Then the above-mentioned studies have some limitations. First, for the streamwise-invariant case ($\alpha = 0$), some essential questions like the influence of the wall flexibility on the amplification of streaks, for instance, has not yet been sufficiently discussed: How does the standing wave interact with the streaks and at what characteristic spanwise scale? Second, how does the amplitude of standing-wave oscillations scale with wall parameters and spanwise wavenumbers β for moderate wall flexibility, and what is the spanwise wavenumber exhibiting oscillatory behavior with highest modulation amplitudes? Third, for the spanwise-invariant case ($\beta = 0$), what are the specific roles of Tollmien-Schlichting waves and traveling-wave flutter modes onto the transient energy growth for short times?

To fill these gaps, we will thus reconsider the transient energy growth problem for fluid flows interacting with a compliant channel, using a Lagrangian approach. It will allow us to overcome the difficulties that arise when summing over the whole spectrum of eigenmodes. The chosen wall model is of Kramer type. We will also adopt the framework described in Ref. [15], where we considered the reduced velocity V_R as the main control parameter for fluid-structure interaction problems [20]. Then, we will discuss the optimal transient energy growth mechanisms for both streamwise-invariant perturbations and disturbances developing in the streamwise–wall-normal plane for a range of reduced velocities and Reynolds numbers.

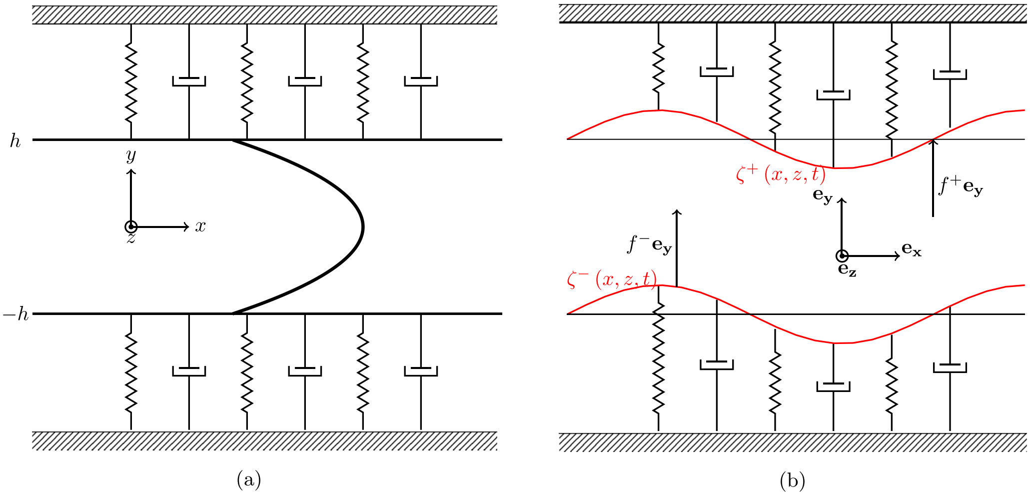

FIG. 1. Channel flow with infinite spring-backed flexible walls. (a) Schematic diagram showing the equilibrium state configuration and (b) wall deformation and coordinate system.

The paper is organized as follows. Section II presents the model and governing equations. In particular, the constrained optimization problem is presented within a Lagrangian framework. The adjoint system of equations, adjoint kinematic conditions, and temporal terminal and initial conditions are given for the linearized fluid-structure interaction system. After having presented the control parameters and the numerical methods in Secs. III and IV, respectively, Sec. V is devoted to give some physical insight into the influence of the reduced velocity and Reynolds number on the short-time dynamics of the perturbation for a range of streamwise and spanwise wavenumbers. Finally, conclusions and prospects are given in the last section.

II. PROBLEM DEFINITION AND SYSTEM OF EQUATIONS

A. Fluid-structure interaction problem

We introduce the Cartesian coordinate system (x, y, z) and unit vectors $(\mathbf{e_x}, \mathbf{e_y}, \mathbf{e_z})$ associated with streamwise, wall-normal, and spanwise directions, respectively. Hereafter, the study will focus on an incompressible Newtonian fluid, with dynamic viscosity μ and density ρ, between two spring-backed deformable plates, which are allowed to move only in the y direction. As shown in previous theoretical analyses [5,19] for a similar case, the wall motion in x and z directions only plays a minor role in the dynamics and is therefore not considered in the present investigation for simplicity of the model. The instantaneous flow velocity and pressure fields are given by $\mathbf{u}(\mathbf{x},t) = (u(\mathbf{x},t), v(\mathbf{x},t), w(\mathbf{x},t))$ and $p(\mathbf{x},t)$, at position $\mathbf{x} = (x,y,z)$ and time t.

Denoting the lower and upper wall positions as $\zeta^\pm(x,z,t)$, the fluid domain corresponds to $\zeta^-(x,z,t) < y < \zeta^+(x,z,t)$ (see Fig. 1), and the flow between the walls follows the incompressible Navier-Stokes equations

$$\frac{\partial \mathbf{u}}{\partial t} + (\mathbf{u}\cdot\nabla)\mathbf{u} = -\frac{1}{\rho}\nabla p + \nu\Delta\mathbf{u}, \tag{1}$$

$$0 = \nabla\cdot\mathbf{u}, \tag{2}$$

where $\nu = \mu/\rho$ denotes the kinematic viscosity. The displacement of the walls is governed by

$$m\frac{\partial^2\zeta^\pm}{\partial t^2} + d\frac{\partial\zeta^\pm}{\partial t} + (B\Delta^2 - T\Delta + K)\zeta^\pm = f^\pm, \tag{3}$$

where m denotes the mass per unit area of the plates, d their damping coefficient, B the flexural rigidity, T the wall tension, K the spring stiffness, and $f^{\pm}$ represents the y component of the hydrodynamic forces acting on the plates. Note that in the above equations $\Delta\mathbf{u} = (\partial_{xx} + \partial_{yy} + \partial_{zz})\mathbf{u}$ while $\Delta\zeta = (\partial_{xx} + \partial_{zz})\zeta$ and $\Delta^2\zeta = (\partial_{x^4} + 2\partial_{x^2z^2} + \partial_{z^4})\zeta$. The fluid-structure interaction problem is completed with the kinematic conditions

$$u = 0, \quad v = \frac{\partial\zeta^{\pm}}{\partial t}, \quad w = 0 \quad \text{for} \quad y = \zeta^{\pm}, \tag{4}$$

associated with no-slip conditions prevailing along the compliant walls.

The unperturbed base configuration corresponds to Poiseuille flow due to a constant pressure gradient within a straight rectangular channel (Fig. 1). It is associated with a steady parabolic streamwise velocity profile $\mathbf{U}(\mathbf{x}) = (U(y), 0, 0)$, with $U(y) = \frac{3}{2}U_m(1 - (y/h)^2)$, between the undeformed walls at $y = \pm h$. Here $U_m = \frac{1}{3}\frac{h^2}{\nu}\mathcal{G}$ is the mean velocity resulting from a constant streamwise pressure gradient $-\mathcal{G}$. Note that we assume a pressure outside the channel walls always equal to the unperturbed pressure $-\mathcal{G}x$ prevailing inside. The same hypothesis is made by Davies and Carpenter [13,21], Tsigklifis and Lucey [19], and few others since then.

B. Linear governing equations

In the next sections, we will investigate the short-time dynamics of a small perturbation superimposed to the equilibrium state. Therefore, the total flow fields are decomposed as

$$\mathbf{u}(\mathbf{x}, t) = U(y)\mathbf{e_x} + \mathbf{u}'(\mathbf{x}, t), \tag{5}$$

$$p(\mathbf{x}, t) = -\mathcal{G}x + p'(\mathbf{x}, t), \tag{6}$$

where $\mathbf{u}'$ and p' represent the deviations from the base flow fields. Similarly, the positions of both walls are written as

$$\zeta^{\pm}(x, z, t) = \pm h + \eta^{\pm}(x, z, t),$$

where $\eta^{\pm}$ measures the displacement of the walls from their equilibrium positions at $y = \pm h$.

The assumption of small-amplitude perturbations leads to the linear version of the Navier-Stokes equations:

$$\frac{\partial\mathbf{u}'}{\partial t} + (\mathbf{U}\cdot\nabla)\mathbf{u}' + U_y v'\mathbf{e_x} = -\frac{1}{\rho}\nabla p' + \nu\Delta\mathbf{u}', \tag{7}$$

$$0 = \nabla\cdot\mathbf{u}'. \tag{8}$$

After linearization of the hydrodynamic forces $f^{\pm}$ (see Ref. [22] for details), the wall equations are recast as

$$\frac{\partial\eta^{\pm}}{\partial t} = \gamma^{\pm}, \tag{9}$$

$$m\frac{\partial\gamma^{\pm}}{\partial t} = -d\gamma^{\pm} - (B\Delta^2 - T\Delta + K)\eta^{\pm} \pm \left(p' - \mu\frac{\partial v'}{\partial y}\right)\Big|_{y=\pm h}, \tag{10}$$

where the wall velocity $\gamma^{\pm} = \partial_t\eta^{\pm}$ has been introduced in order to obtain a system of first-order differential equations in time. This system of linear partial differential equations is completed with the associated linearized kinematic conditions:

$$u' = -\eta^{\pm}\frac{dU}{dy}, \quad v' = \gamma^{\pm}, \quad w' = 0 \quad \text{at} \quad y = \pm h. \tag{11}$$

See our previous paper [15] for further details about the derivation of the governing equations for small-amplitude perturbations.

C. Optimization framework

For the sake of conciseness, we henceforth omit the prime for the small-amplitude perturbations. We first introduce a measure of the total energy of the perturbation in a computational box of size $L_x \times 2h \times L_z$:

$$E(\mathbf{u}) = \underbrace{\langle\langle \rho \mathbf{u}^2 \rangle\rangle}_{\text{Fluid kinetic energy}} + \underbrace{\sum_{i=\pm} \langle B(\Delta\eta^i)^2 + T\nabla\eta^i \cdot \nabla\eta^i + K(\eta^i)^2 \rangle}_{\text{Wall potential energy}} + \underbrace{\sum_{i=\pm} \langle m(\gamma^i)^2 \rangle}_{\text{Wall kinetic energy}}, \tag{12}$$

where $\langle\langle \cdot \rangle\rangle = \int_0^{L_x} \int_{-h}^{h} \int_0^{L_z} \cdot \, \mathrm{d}x \, \mathrm{d}y \, \mathrm{d}z$ and $\langle \cdot \rangle = \int_0^{L_x} \int_0^{L_z} \cdot \, \mathrm{d}x \, \mathrm{d}z$, which represent the integral values either over the whole domain D or along the walls ∂D. Here, E may be written as a function of $\mathbf{u}$ only since $\eta^{\pm}$ and $\gamma^{\pm}$ can be expressed in terms of the velocity components at the walls using kinematic conditions (11). In Eq. (12), we separate the energy contributions from the walls (i.e., wall potential energy and wall kinetic energy) from the one associated with the fluid (i.e., fluid kinetic energy). This decomposition is also used by Hœpffner *et al.* [17] and Malik *et al.* [12] for transient growth analysis of flows interacting with compliant walls.

The largest total transient energy growth E that a small perturbation can experience over a fixed target time τ is obtained by maximizing the following constrained Lagrangian:

$$\begin{aligned}
\mathcal{L} = {} & E(\mathbf{u}(t=\tau)) - \rho \int_0^{\tau} \left\langle\!\!\left\langle \mathbf{a} \cdot \left(\mathbf{u}_t + \mathbf{U} \cdot \nabla \mathbf{u} + \frac{1}{\rho} \nabla p - \nu \Delta \mathbf{u} + v U_y \mathbf{e_x} \right) \right\rangle\!\!\right\rangle \mathrm{d}t - \int_0^{\tau} \langle\langle \Pi \nabla \cdot \mathbf{u} \rangle\rangle \mathrm{d}t \\
& - \int_0^{\tau} \langle g^+ [m\gamma_t^+ + d\gamma^+ + (B\Delta^2 - T\Delta + K)\eta^+ - p^+ + \mu v_y^+] \rangle \mathrm{d}t \\
& - \int_0^{\tau} \langle g^- [m\gamma_t^- + d\gamma^- + (B\Delta^2 - T\Delta + K)\eta^- + p^- - \mu v_y^-] \rangle \mathrm{d}t \\
& - \int_0^{\tau} \langle e^+ [\eta_t^+ - \gamma^+] \rangle \mathrm{d}t - \int_0^{\tau} \langle e^- [\eta_t^- - \gamma^-] \rangle \mathrm{d}t \\
& - \langle\langle \mathbf{a}_0 \cdot [\mathbf{u}(t=0) - \mathbf{u}_0] \rangle\rangle - \lambda [E(\mathbf{u}_0) - 1],
\end{aligned} \tag{13}$$

where the control is $\mathbf{u}_0 = (u_0, v_0, w_0)$ and $u_0^{\pm} = -\eta_0^{\pm} U_y|_{\pm=h}$, $v_0^{\pm} = \gamma_0^{\pm}$, $w_0^{\pm} = 0$. In Eq. (13), λ, $\mathbf{a}_0$, Π, $\mathbf{a}$, g^+, g^-, e^+, and e^- are the Lagrange multiplier fields imposing the constraints that the initial total perturbation energy equals 1, the perturbation is incompressible, and that the fluid-structure interaction system (10) is satisfied.

Taking variations with respect to all the degrees of freedom, where the boundary conditions are included implicitly when integrating by parts the momentum equations, leads to the adjoint evolution equations for the fields,

$$\begin{aligned}
& -\mathbf{a}_t - \mathbf{U} \cdot \nabla \mathbf{u} + \frac{1}{\rho} \nabla \Pi - \nu \Delta \mathbf{u} + a U_y \mathbf{e_y} = 0, \\
& \nabla \cdot \mathbf{a} = 0, \\
& -m g_t^+ - e^+ + g^+ d - \Pi^+ + \mu b_y^+ = 0, \\
& -m g_t^- - e^- + g^- d + \Pi^- - \mu b_y^- = 0, \\
& -e_t^+ + (B\Delta^2 - T\Delta + K) e^+ - \mu a_y^+ U_y^+ = 0, \\
& -e_t^- + (B\Delta^2 - T\Delta + K) e^- + \mu a_y^- U_y^- = 0,
\end{aligned} \tag{14}$$

together with the adjoint kinematic conditions,

$$\begin{aligned}
& g^- = b^-, \quad g^+ = b^+, \\
& a^+ = 0, \quad a^- = 0,
\end{aligned} \tag{15}$$

the temporal terminal conditions,

$$\text{for } D\setminus\partial D: \mathbf{a}(t=\tau)=2\mathbf{u}(t=\tau),$$
$$\text{and for } \partial D: g^{\pm}(t=\tau)=2\gamma^{\pm}(t=\tau),\ e^{\pm}(t=\tau)=2\big[2\rho h U_y|^2_{\pm h}+(B\Delta^2-T\Delta+K)\big]\eta^{\pm}(t=\tau), \tag{16}$$

and the initial conditions,

$$\text{for } D\setminus\partial D: \mathbf{a}(t=0)=2\lambda\mathbf{u}(t=0),$$
$$\text{and for } \partial D: g^{\pm}(t=0)=2\lambda\gamma^{\pm}(t=0),\ e^{\pm}(t=0)=2\lambda\big[2\rho h U_y|^2_{\pm h}+(B\Delta^2-T\Delta+K)\big]\eta^{\pm}(t=0), \tag{17}$$

where the Lagrange multiplier λ is fixed to verify unit total energy at $t=0$. Here, the integration along the wall-normal direction is computed with spectral accuracy. A direct and adjoint looping method [23], where the direct system is integrated forward in time and the adjoint problem is advanced backward in time, is hence used to compute the optimal initial perturbation for a given target time τ. A similar technique has already been used for a Couette flow by our team with the same code [24]. In the next sections, the corresponding maximum energy growth is referenced as $G(\tau)$. Since the nonlinear terms are removed from the equations, both direct and adjoint systems can be solved in Fourier space, without any coupling between spatial Fourier modes. In this context, we introduce the following waveform for the different fields:

$$\mathbf{u}(x,y,z,t)=\widetilde{\mathbf{u}}(y,t)e^{j(\alpha x+\beta z)}+\text{c.c.},\quad \mathbf{a}(x,y,z,t)=\widetilde{\mathbf{a}}(y,t)e^{j(\alpha x+\beta z)}+\text{c.c.},$$
$$\gamma^{\pm}(x,z,t)=\widetilde{\gamma}^{\pm}(t)e^{j(\alpha x+\beta z)}+\text{c.c.},\quad \eta^{\pm}(x,z,t)=\widetilde{\eta}^{\pm}(t)e^{j(\alpha x+\beta z)}+\text{c.c.},$$
$$g^{\pm}(x,z,t)=\widetilde{g}^{\pm}(t)e^{j(\alpha x+\beta z)}+\text{c.c.},\quad e^{\pm}(x,z,t)=\widetilde{e}^{\pm}(t)e^{j(\alpha x+\beta z)}+\text{c.c.},$$

with $\sqrt{j}=-1$ and α and β the streamwise and spanwise wavenumbers, respectively. Again, for simplicity, we omit $\widetilde{\cdot}$ in the following.

III. CONTROL PARAMETERS

In the present study, the compliant-channel flow system is characterized by nine dimensional parameters: the volumetric flow rate $[Q]=\text{m}^2\,\text{s}^{-1}$, the half height of the channel, $[h]=\text{m}$, the fluid density $[\rho]=\text{kg}\,\text{m}^{-3}$, the kinematic viscosity $[\nu]=\text{m}^2\,\text{s}^{-1}$, the mass of the plate per unit area, $[m]=\text{kg}\,\text{m}^{-2}$, the damping coefficient of the wall, $[d]=\text{kg}\,\text{m}^{-2}\,\text{s}^{-1}$, the bending stiffness of the plate, $[B]=\text{kg}\,\text{m}^2\,\text{s}^{-2}$, the wall tension $[T]=\text{kg}\,\text{s}^{-2}$, and the spring stiffness $[K]=\text{kg}\,\text{m}^{-2}\,\text{s}^{-2}$. Hence, the system may be described by six dimensionless parameters:

$$\text{Re}=\frac{Q}{\nu},\quad V_R=\frac{Q}{4h^2}\sqrt{\frac{m}{K}},\quad \Gamma=\frac{m}{\rho h},$$
$$d_*=\frac{d}{\sqrt{mK}},\quad B_*=\frac{B}{Kh^4},\quad T_*=\frac{T}{Kh^2}. \tag{18}$$

Here Re is the Reynolds number based on channel diameter and average flow velocity. The nondimensional wall parameters d_*, B_*, and T_* are relative to the spring stiffness K. Finally, two nondimensional parameters account for the coupling between the fluid and the compliant walls: the mass ratio between the walls and the fluid, Γ; and the reduced velocity V_R that represents the ratio of the wall characteristic timescale $\sqrt{m/K}$ to the characteristic flow advection timescale $4h^2/Q$ (see Refs. [15,20]). In order to reduce the dimensionality of the control parameter space, and without much loss of generality, we only use $T=0$ and $\Gamma=2$ hereafter, and we also set three dimensional parameters at $\rho=1$, $h=1$, and $Q=1$.

IV. NUMERICAL METHODS

The numerical method is here described for the direct system only, since time marching of the adjoint system proceeds in a similar fashion. The approach closely matches the Uzawa algorithm described by Peyret [25]. Spatial directions are approximated with spectral accuracy and a semi-implicit second-order time-marching scheme is used.

As usually done in the incompressible regime, a P_N/P_{N-2} Chebyshev collocation method is used for the spatial discretization. We rewrite the system of equations in vector form with complex components, using $\mathbf{u} = (u_1, u_2, \dots, u_N)$, $\mathbf{v} = (v_1, v_2, \dots, v_N)$, and $\mathbf{w} = (w_1, w_2, \dots, w_N)$ for velocity components and $\mathbf{p} = (p_2, \dots, p_{N-1})$ for the pressure. We also introduce $\widetilde{\mathbf{u}} = (u_2, \dots, u_{N-1})$ and $\widetilde{\mathbf{v}} = (v_2, \dots, v_{N-1})$, where only the interior points are included. After spatial discretization, with N Chebyshev collocation points, the first and second y-derivative operators acting on velocity fields are recast as $\mathbf{D}$ and $\mathbf{D}^2$ matrices, respectively. The y-derivative operator on the $N-2$ grid points for the pressure is represented by matrix $\mathbf{D}_p$. Finally, we note hereafter the time step Δt and n the number of the time iteration.

The discrete system of the momentum equations for the fluid is then rewritten in matrix form to yield

$$\begin{aligned}
\mathbf{M}\widetilde{\mathbf{u}}^{n+1} - j\alpha\mathbf{p}^{n+1} &= \widetilde{\mathbf{S}}_u^{n+1,n,n-1},\\
\mathbf{M}\widetilde{\mathbf{v}}^{n+1} - \mathbf{D}_p\mathbf{p}^{n+1} &= \widetilde{\mathbf{S}}_v^{n+1,n,n-1},\\
\mathbf{M}\widetilde{\mathbf{w}}^{n+1} - j\beta\mathbf{p}^{n+1} &= \mathbf{S}_w^{n,n-1},
\end{aligned} \tag{19}$$

and the divergence-free constraint expressed at the interior points reads

$$\widetilde{\mathbf{D}}\widetilde{\mathbf{v}}^n + j\alpha\widetilde{\mathbf{u}}^n + j\beta\widetilde{\mathbf{w}}^n = \mathbf{S}_d^n, \tag{20}$$

where $\mathbf{M} = \nu\widetilde{\mathbf{D}}^2 - \sigma\mathbf{I}$ with $\sigma = 3/(2\Delta t) + \nu(\alpha^2 + \beta^2)$. Here $\widetilde{\mathbf{D}}$ and $\widetilde{\mathbf{D}}^2$ represent the first and second derivative operators on N grid points, where the first and/or last rows and first and/or last columns are removed. In Eqs. (19) and (20), boundary conditions for u and v are included on the right-hand side of the equations. The boundary conditions are time dependent. As a consequence, in Eq. (20) we have

$$\mathbf{S}_d^n = -\big(D_{11}v_1^n + D_{1N}v_N^n, D_{21}v_1^n + D_{2N}v_N^n, \dots, D_{N1}v_1^n + D_{NN}v_N^n\big).$$

For Eqs. (19), we use the following decomposition:

$$\widetilde{\mathbf{S}}_u^{n+1,n,n-1} = \mathbf{S}_u^{n,n-1} + \mathbf{C}_u^{n+1}, \quad \widetilde{\mathbf{S}}_v^{n+1,n,n-1} = \mathbf{S}_v^{n,n-1} + \mathbf{C}_v^{n+1},$$

with

$$\begin{aligned}
\mathbf{S}_u^{n,n-1} &= -(4\widetilde{\mathbf{u}}^n - \widetilde{\mathbf{u}}^{n-1})/2\Delta t + 2\mathbf{f}_u^n - \mathbf{f}_u^{n-1},\\
\mathbf{S}_v^{n,n-1} &= -(4\widetilde{\mathbf{v}}^n - \widetilde{\mathbf{v}}^{n-1})/2\Delta t + 2\mathbf{f}_v^n - \mathbf{f}_v^{n-1},\\
\mathbf{S}_w^{n,n-1} &= -(4\widetilde{\mathbf{w}}^n - \widetilde{\mathbf{w}}^{n-1})/2\Delta t + 2\mathbf{f}_w^n - \mathbf{f}_w^{n-1},
\end{aligned}$$

where

$$\mathbf{f}_u^n = j\alpha\widetilde{\mathbf{U}}\widetilde{\mathbf{u}}^n + \widetilde{\mathbf{v}}^n\widetilde{\mathbf{U}}_y, \quad \mathbf{f}_v^n = j\alpha\widetilde{\mathbf{U}}\widetilde{\mathbf{v}}^n, \quad \mathbf{f}_w^n = j\beta\widetilde{\mathbf{U}}\widetilde{\mathbf{w}}^n,$$

and the contribution of the boundary conditions for the second derivatives are included into

$$\mathbf{C}_u^n = -\big(D_{11}^2u_1^n + D_{1N}^2u_N^n, D_{21}^2u_1^n + D_{2N}^2u_N^n, \dots, D_{N1}^2u_1^n + D_{NN}^2u_N^n\big),$$

$$\mathbf{C}_v^n = -\big(D_{11}^2v_1^n + D_{1N}^2v_N^n, D_{21}^2v_1^n + D_{2N}^2v_N^n, \dots, D_{N1}^2v_1^n + D_{NN}^2v_N^n\big).$$

Applying the divergence operator (20) onto the momentum equations (19), an equation for the pressure is obtained:

$$\mathbf{Q}\mathbf{p}^{n+1} = \mathbf{G}^{n,n-1} + \mathbf{H}^{n+1}, \tag{21}$$

with $\mathbf{Q} = \alpha^2\mathbf{M}^{-1} - \widetilde{\mathbf{D}}\mathbf{M}^{-1}\mathbf{D}_p + \beta^2\mathbf{M}^{-1}$ and

$$\begin{aligned}\mathbf{G}^{n,n-1} &= j\alpha\mathbf{M}^{-1}\mathbf{S}_u^{n,n-1} + \widetilde{\mathbf{D}}\mathbf{M}^{-1}\mathbf{S}_v^{n,n-1} + j\beta\mathbf{M}^{-1}\mathbf{S}_w^{n,n-1},\\ \mathbf{H}^{n+1} &= -\mathbf{S}_d^{n+1} + j\alpha\mathbf{M}^{-1}\mathbf{C}_u^{n+1} + \widetilde{\mathbf{D}}\mathbf{M}^{-1}\mathbf{C}_v^{n+1}.\end{aligned}$$

Following Davies and Carpenter [21], a three-point implicit time discretization for the wall equations is used to ensure numerical stability:

$$\begin{aligned}&m(3\gamma_\pm^{n+1} - 4\gamma_\pm^n + \gamma_\pm^{n-1}) = 2\Delta t\big[-d\gamma_\pm{}^{n+1} - (B\Delta^2 + K)\eta_\pm{}^{n+1} \pm p_{1/N}^{n+1} \mp \mu(\mathbf{D}\mathbf{v})_{1/N}{}^{n+1}\big],\\ &(3\eta_\pm^{n+1} - 4\eta_\pm^n + \eta_\pm^{n-1}) = 2\Delta t\gamma_\pm^{n+1},\end{aligned} \tag{22}$$

with $\Delta^2 = \alpha^4 + \beta^4 + 2\alpha^2\beta^2$ and where p_1 and p_N are computed using spectral extrapolation. The following system is then solved iteratively at each time step:

$$\begin{aligned}&\mathbf{p}^{n+1,k+1} = \mathbf{Q}^{-1}[\mathbf{G}^{n,n-1} + \mathbf{H}^{n+1,k}],\\ &\tilde{\mathbf{u}}^{n+1,k+1} = \mathbf{M}^{-1}j\alpha\mathbf{p}^{n+1,k+1} + \mathbf{M}^{-1}\big[\mathbf{S}_u^{n,n-1} + \mathbf{C}_u^{n+1,k}\big],\\ &\tilde{\mathbf{v}}^{n+1,k+1} = \mathbf{M}^{-1}\mathbf{D}_p\mathbf{p}^{n+1,k+1} + \mathbf{M}^{-1}\big[\mathbf{S}_v^{n,n-1} + \mathbf{C}_v^{n+1,k}\big],\\ &\mathbf{w}^{n+1,k+1} = \mathbf{M}^{-1}j\beta\mathbf{p}^{n+1,k+1} + \mathbf{M}^{-1}\mathbf{S}_w^{n,n-1},\\ &\gamma_\pm^{n+1,k+1}\left[1 + \frac{2\Delta t}{3m}d\right] + \eta_\pm^{n+1,k+1}\left[\frac{2\Delta t}{3m}(B\Delta^2 + K)\right]\\ &\quad = \frac{2\Delta t}{3m}\big[\pm p_{1/N}^{n+1,k+1} \mp \mu(\mathbf{D}\mathbf{v})_{1/N}^{n+1,k+1}\big] + \frac{4}{3}\gamma_\pm^n - \frac{1}{3}\gamma_\pm^{n-1},\\ &\eta_\pm^{n+1,k+1} - \frac{2}{3}\Delta t\gamma_\pm^{n+1,k+1} = \frac{4}{3}\eta_\pm^n - \frac{1}{3}\eta_\pm^{n-1}.\end{aligned} \tag{23}$$

In Eqs. (23), the wall part is easily solved by inverting a 2×2 system and the boundary conditions for the velocity components are updated using kinematic conditions. Between 20 and 50 iterations are needed at each time step to converge.

Finally, the numerical method is further improved by considering separately perturbations of sinuous or varicose symmetries and using only half of the channel together with derivative operators appropriate for the symmetry of each component of the different flow fields [26]. The separation between varicose and sinuous cases facilitates the analysis of the driving mechanisms of the dynamics and also allows to run the different symmetries simultaneously on two processors. The present code is an extension of a direct numerical simulation (DNS) code developed by our team which has been well validated for channel and Couette flow simulations with rigid walls [24,27].

V. NUMERICAL VALIDATION

A. Asymptotic case

In this section, we validate the numerical method for time marching the linearized Navier-Stokes equations that include the wall deformation (referenced as LDNS hereafter). Both the direct and adjoint systems are considered. For that purpose, we focus on a case described in a previous paper of our team. The control parameters are fixed to $V_R = 1$, $B_* = 4$, $d_* = 0$, $\alpha = 1$, and $\mathrm{Re} = 10\,000$. For this case, the long-time dynamics is driven by the varicose traveling-wave flutter mode. The linear stability problem has been solved using an algebraic eigenvalue solver. The LDNS is initialized with a random noise. The numerical parameters are fixed to $N = 60$ and $\Delta t = 0.01$. Results are shown in

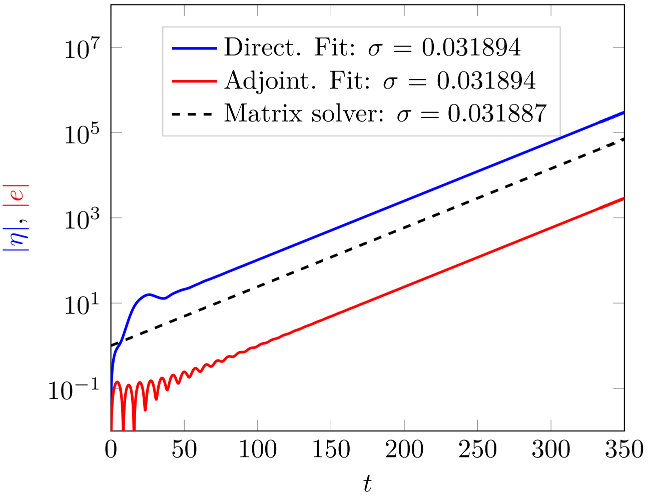

FIG. 2. Validation of the time-marching linear solver for both direct and adjoint formulations for $\mathrm{Re} = 10\,000$, $\alpha = 1$, $B_* = 4$, $\Gamma = 2$, $d_* = 0$, and $V_R = 1$. Numerical parameters are set to $N = 60$ and $\Delta t = 0.01$. The time evolution of the modulus of the wall vertical displacement for a given random initial perturbation is shown on a logarithmic scale. A linear regression provides a temporal growth rate $\sigma = 0.031894$ for both direct and adjoint solvers. The temporal evolution of the most amplified linear eigenvalues obtained with the eigenvalue matrix solver gives $\sigma = 0.031887$.

Fig. 2, where we have reported the time evolution of the modulus of the wall vertical displacement for both the direct (η) and adjoint systems (e). The figure shows a perfect agreement between the temporal amplification rate obtained with the algebraic eigenvalue solver and the one derived from the linearized Navier-Stokes solver for both the direct and adjoint problems.

In Fig. 3, we also compare the spatial structure of the eigenmodes computed with the eigenvalue solver and the LDNS for the direct system, which again perfectly agree.

B. Transient growth

The coupling between the direct and adjoint solvers and the choice of the energy norm are discussed using results given by Hœpffner *et al.* [17]. For that purpose, we convert the dimensionless values provided by Hœpffner *et al.* [17] to those used in the present paper. Hence, for this case, the reduced velocity is fixed to $V_R = 23.57$, the flexural rigidity is set to $B_* = 4$, the wall dissipation $d_* = 0.0071$, and the Reynolds number $\mathrm{Re} = 6667$. The spanwise and streamwise wavenumbers are fixed to 0.2 and 0, respectively. Two different energy norms are used: the total energy norm (12) and another one based only on the flow kinetic energy inside the domain. The envelopes of the optimal gain G over the target time τ computed using the direct-adjoint looping method for both energy norms are shown in Fig. 4. The number of collocation points used is $N = 60$ and the time step is fixed to $\Delta t = 0.01$. Published results of Hœpffner *et al.* [17] are also reported. The envelope G is either associated with the sinuous or varicose symmetry depending on the chosen time horizon used for the optimization. Figure 4 shows an almost perfect agreement between our time-stepping algorithm and the matrix solver used by Hœpffner *et al.* [17]. Hœpffner *et al.* [17] have used an eigenfunctions basis for the computation of G. The authors have been unable to obtain a true convergence towards the optimal solution when including too many modes in the projection. Especially when considering the whole spectrum, the authors show that the optimal gain tends to blow up. Within the present time-stepping framework, we do not observe any problem for the convergence even when doubling the number of collocation points. It seems therefore more appropriate to use the present method in order to draw definite conclusions about transient growth

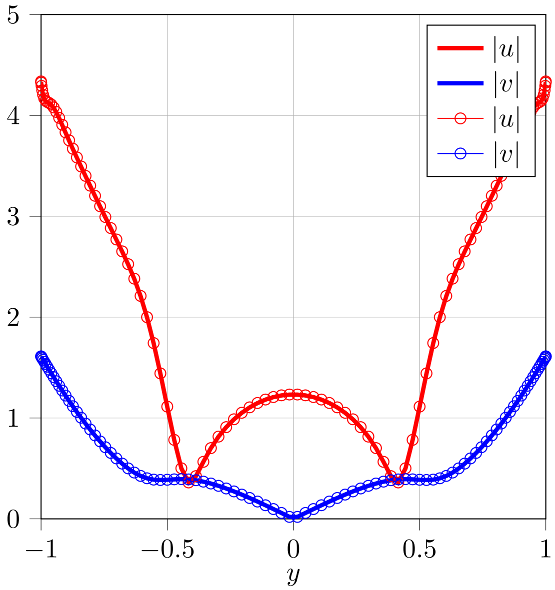

FIG. 3. Same flow case as in Fig. 2. The envelope of the eigenfunctions computed either with the LDNS (in solid lines) or the eigenvalue solver (open circles) are shown.

scenarios investigated hereafter. The figure also shows that while a similar beating phenomenon is recovered for both inner products, the amplitude of the perturbation is clearly decreased by using the fluid kinetic energy norm only. Therefore, it seems inappropriate to restrict the analysis to the fluid kinetic energy only because it fails to take into account a significant level of amplification associated with the wall dynamics. Hereafter, all computations are carried out using the total energy norm. In the next section, the wall dissipation is set to zero and the flexural rigidity is fixed to $B_* = 1$ for illustration purposes.

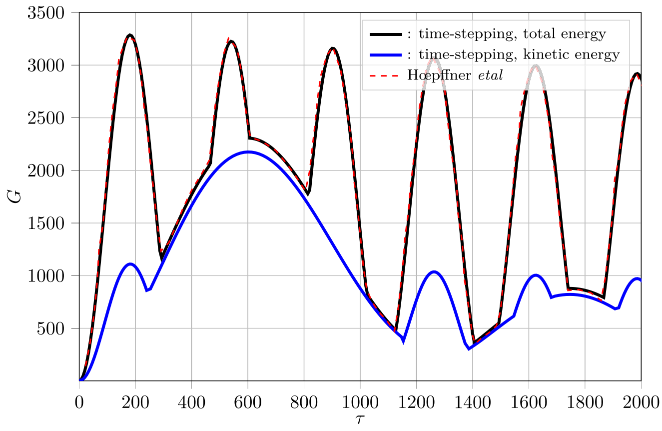

FIG. 4. G as a function of the target time τ for $V_R = 23.57$, $B_* = 4$, $d_* = 0.0071$, $\mathrm{Re} = 6667$, $\beta = 0.2$, and $\alpha = 0$. Results extracted from Hœpffner *et al.* [17] are also reported. Computations associated with the total energy norm and the fluid kinetic energy norm inside the domain are shown in black and blue, respectively.

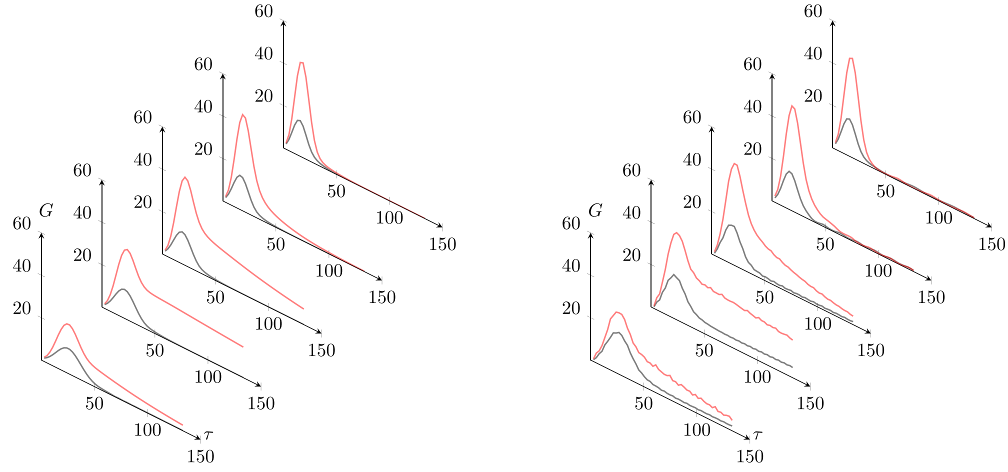

(a) $V_R = 0.006$ (b) $V_R = 0.45$

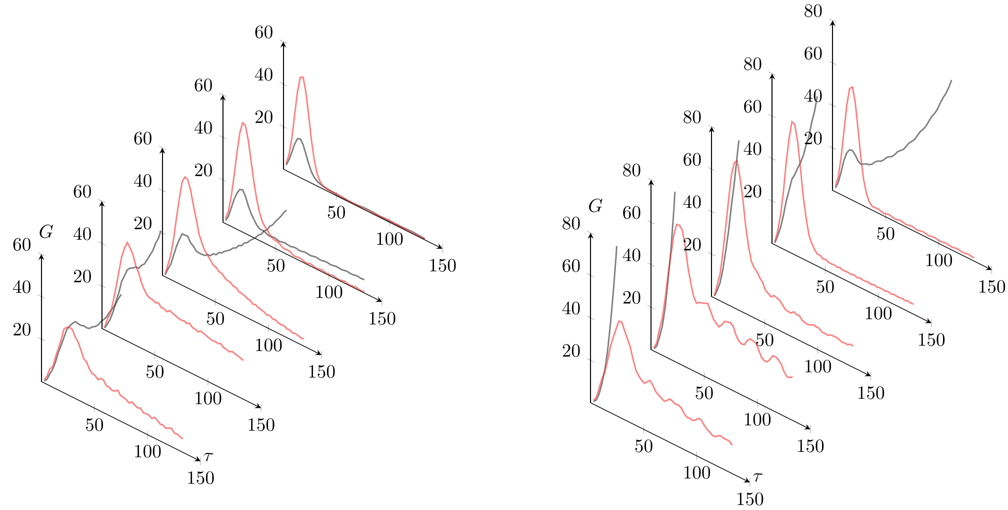

(c) $V_R = 0.53$ (d) $V_R = 065$

FIG. 5. G as a function of the target time τ for Re $= 6666$ and (a) $V_R = 0.006$, (b) $V_R = 0.45$, (c) $V_R = 0.53$, and (d) $V_R = 0.65$. For all panels, the streamwise wavenumbers are $\alpha = 0.8$, 1, 1.2, 1.4, and 1.6 (from the left to the right). Red, sinuous symmetry; black, varicose symmetry.

VI. RESULTS

A. Optimal growth for $\beta = 0$

In this section, the analysis is restricted to two-dimensional perturbations with vanishing spanwise wavenumber, $\beta = 0$. In Fig. 5, time evolutions of G for various streamwise wavenumbers are shown at different reduced velocity for both the sinuous and varicose symmetries. The figure shows that for V_R varying from $V_R = 0.006$ to $V_R = 0.45$, a weak effect of the wall flexibility is observed for all α that are investigated. When the reduced velocity is increased up to 0.53, the varicose configuration is driven by the asymptotically unstable TWF mode for short times for $\alpha = 0.8$ and 1. One may recall that the varicose case is the most unstable one when considering the asymptotic regime (i.e., the critical reduced velocity is lower than the one associated with the sinuous case [15]).

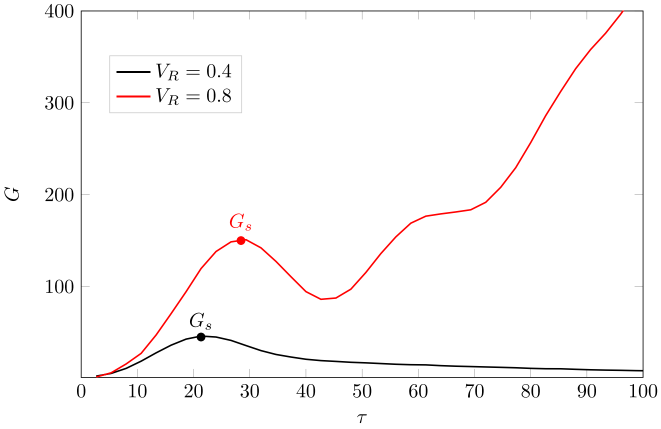

FIG. 6. G as a function of the target time τ for $\mathrm{Re} = 6666$, $\alpha = 1.2$, and $V_R = 0.4,\ 0.8$.

For $\alpha = 1.2$, 1.4, and 1.6, a distinct short-time growth is observed with the emergence of a distinct peak in G. For these cases, the sinuous configuration is always the most amplified for short times. For $V_R = 0.65$ and the varicose symmetry, the system is mainly governed by the unstable mode for $\alpha = 0.8,\ 1.2$, and 1.4. A distinct peak of G is only observed for $\alpha = 1.6$. Once again, for this streamwise wavenumber, the sinuous symmetry is the most amplified symmetry for short times. In particular, its energy peak in G is seen to increase with the reduced velocity. Hence, focusing our attention on the transient growth mechanism, the sinuous configuration seems to be the most interesting case to investigate. In addition, the sinuous case also exhibits a clear distinct low-frequency beating, not observed for the varicose symmetry [see Fig. 5(d) and $\alpha = 1$]. As a consequence, for the sake of conciseness, we will focus on the sinuous symmetry hereafter.

The influence of the reduced velocity onto the optimal gain G is further illustrated in Fig. 6 for $\alpha = 1.2$, $\mathrm{Re} = 6666$, and target times varying from 0 to 100. We recall that for this Reynolds number, the TS modes are temporally damped for the rigid-wall case. For $V_R = 0.4$, G exhibits a growth for short times and relaxes to zero in the asymptotic regime. For $V_R = 0.8$, G peaks during short times before being damped until $\tau = 25$ and then increases for long times. For this reduced velocity value, the TWF mode is temporally amplified. To further characterize the energy growth for short times, we note G_s, the optimal gain associated with the first peak (see Fig. 6). In Fig. 6, it is clear that G_s depends on V_R. The knowledge of the impact of V_R on G_s is also of strong interest even in the slightly supercritical regime since it provides some information on the receptivity of the system to external disturbances.

Let us now introduce the quantity $G_s^M(\mathrm{Re}, V_R) = \max_\alpha G_s(\mathrm{Re}, V_R, \alpha)$ that measures the maximum gain reached by G_s over α for a given configuration (Re, V_R). The distribution of G_s^M with Re and V_R is shown in Fig. 7(a) and the associated optimal wavenumber α_s^M in Fig. 7(b).

Figure 7 shows that while the TS wave is slightly damped temporally [13] for small values of V_R, the transient growth is enhanced with the wall compliance. In addition, close to the critical value of V_R for the onset of the TWF mode, the transient growth for short times has considerably increased.

Let us now focus on some representative cases. In Fig. 8, the time evolutions of the total energy associated with the optimal initial perturbation for $V_R = 0.6$, $\mathrm{Re} = 8300$, and some target times τ and streamwise wavenumbers α are displayed. For comparison purposes, the envelope G for the rigid case is also reported (in red). The case is represented by a black dot in the maps of Fig. 7. The figure shows that the distribution of the total energy gain for short times is in strong contrast with the rigid-wall counterpart. The compliant walls can either stabilize or enhance the energy growth. One may also notice that energy growth exhibits beating oscillations for some parameters.

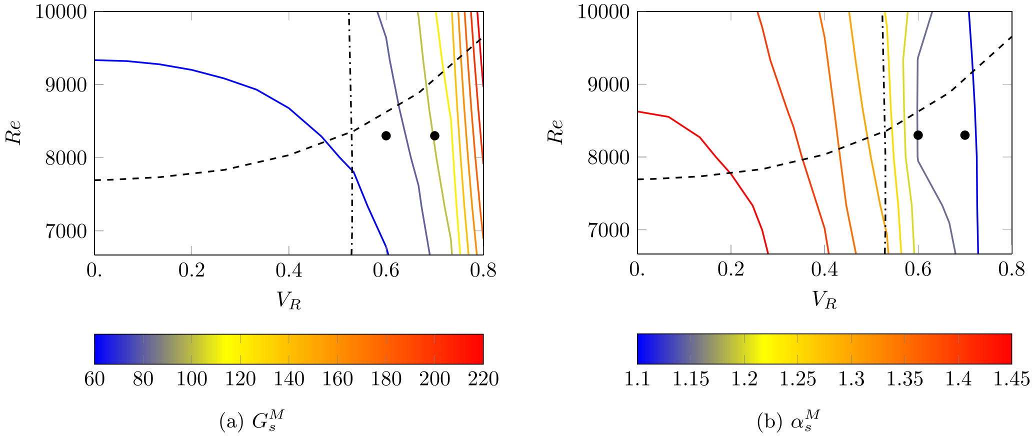

(a) G_s^M

(b) α_s^M

FIG. 7. Isocontours of (a) G_s^M and (b) α_s^M in the (Re, V_R) plane. The dashed line denotes the evolution of the critical Reynolds number with respect to the TS mode. The dash-dotted line represents the evolution of the critical reduced velocity with respect to the TWF mode.

The same analysis is conducted for $V_R = 0.7$ and results are shown in Fig. 9 (the case is also reported in the maps of Fig. 7). The figure shows a similar behavior as the one observed for $V_R = 0.6$ with the exception that the amplitude of the oscillations and the total energy peak G_s^M are enhanced by the wall compliance. Interestingly, the figure also shows that the onset of the exponential instability for the TWF mode occurs at different streamwise wavenumbers from those where the largest oscillations are observed. In an effort to explain the underlying mechanism we show in Fig. 10 a subset of the eigenvalue spectrum for $V_R = 0.7$ and $\alpha = 1$. The complex circular frequency is noted as $\omega = \omega_r + j\omega_i$ with the frequency $\omega_r/2\pi$ and the temporal amplification rate ω_i. In addition to the TS mode, the spectrum exhibits also two distinct modes, the so-called traveling-wave flutter (TWF) modes (see Ref. [15] for further results). One TWF mode is traveling along the downstream direction in x. The other one is traveling in the opposite direction. In Fig. 10, we have also reported the distance between the circular frequency of the TWF mode traveling in the downstream direction and the one associated with the TS mode, labeled $\Delta\omega$. The difference $\Delta\omega$ is seen to be correlated with the time period of the beating process, ΔT, observed in Fig. 9: ΔT is nearly equal to $2\pi/\Delta\omega$. This behavior has also been observed by Davies and Carpenter [21]. It is a consequence of constructive interference between the TS and TWF waves. This interpretation is further illustrated in Fig. 11, where the distributions of ω_r and ω_i with α are shown for both TWF and TS modes. The figure shows that for the range in α where the oscillating behavior is observed in Fig. 9, circular frequencies associated with TS and TWF waves are closely approaching each other. In this region, the two modes have very similar eigenfunctions (i.e., they are nonorthogonal) and their superposition generates an energy growth and a low-frequency beating.

To gain insight into the role of the different modes on the time evolution of $E(t)$, the optimal initial perturbation is expanded onto the basis of eigenvectors. Let us note the initial perturbation $\mathbf{q}_i = \mathbf{V}\hat{\mathbf{a}}$ with $\mathbf{V} = (\hat{\mathbf{q}}_1, \hat{\mathbf{q}}_2, \dots, \hat{\mathbf{q}}_m)$ the m columns containing the discrete eigenvectors (the corresponding eigenvalues are noted $-j\omega_i$, hereafter) and $\hat{\mathbf{a}}$ the vector containing the coefficients of the expansion of $\mathbf{q}_i$. To find $\hat{\mathbf{a}}$, we use an orthogonal projection based on a Gram-Schmidt orthonormalization process. It is equivalent to require that the projection error is orthogonal to the set of eigenmodes for the chosen subspace of dimension m. The procedure is further detailed in Ref. [28]. The time evolution of $\mathbf{q}_i$ expanded into an eigenmode basis reads $\mathbf{q}_i(t) = \mathbf{V}\mathbf{a}(t)$ with $\mathbf{a}(t) = (\hat{a}_1 e^{-j\omega_1 t}, \hat{a}_2 e^{-j\omega_2 t}, \dots, \hat{a}_m e^{-j\omega_m t})$.

We now consider two representative cases for Re $= 8300$, $\alpha = 1$, and $\tau = 26$. The reduced velocity is fixed either to $V_R = 0.6$ or $V_R = 0.7$. Three subsets of modes are investigated and their

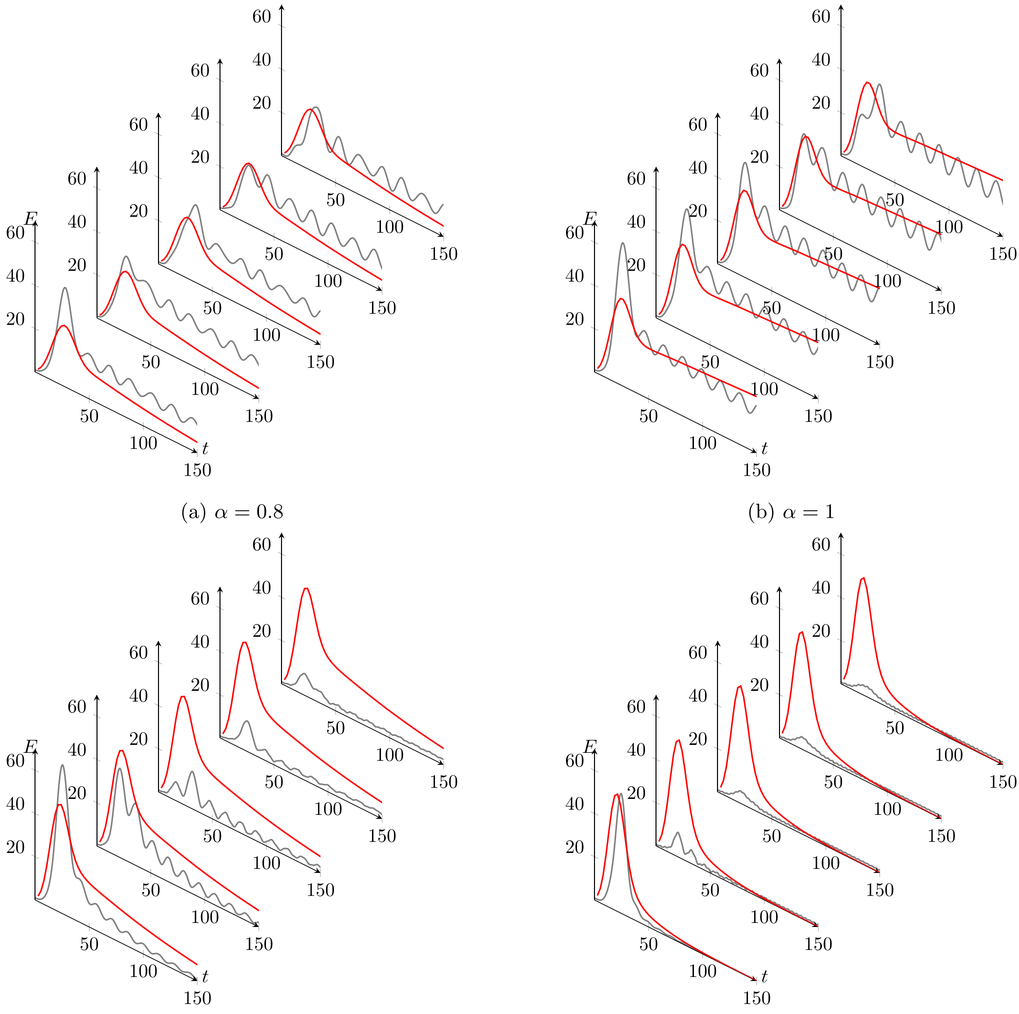

(a) $\alpha = 0.8$ (b) $\alpha = 1$ (c) $\alpha = 1.2$ (d) $\alpha = 1.4$

FIG. 8. Time evolution of the total energy for the optimal initial perturbation for $\tau = 26$, 66, 133, 200, 266 (from the left to the right) and $\alpha = 0.8$, 1, 1.2, 1.4. The Reynolds number is fixed to Re $= 8300$ and the reduced velocity is set to $V_R = 0.6$. In red, the envelope G for the rigid case is represented.

dimensions are fixed to $m = 16$. A first subset includes the least damped modes. A second subset includes also the least damped modes but the TWF mode propagating downstream is removed. For the last subset, the TS mode is removed. Time evolutions of the reduced-order models are compared to LDNS results in Fig. 12. The time evolution of the kinetic energy associated with the optimal initial perturbation for the rigid-wall case is also reported in the figure for the same parameters for comparison purposes. For both reduced velocities, the figure shows an almost perfect match between $E(t)$ extracted from the LDNS and $E(t)$ obtained by using the first subspace of modes (i.e., including both TWF and TS modes). It validates the orthogonal projection used in the present study. When the reduced-order model excludes the TWF mode propagating downstream it has as a consequence that the oscillations disappear, as expected. The total energy peak for short time is also reduced. For $V_R = 0.6$, and for large times, the dynamics is mainly driven by the TS mode. For this value of the reduced velocity, the total energy associated with the full system is seen to oscillate

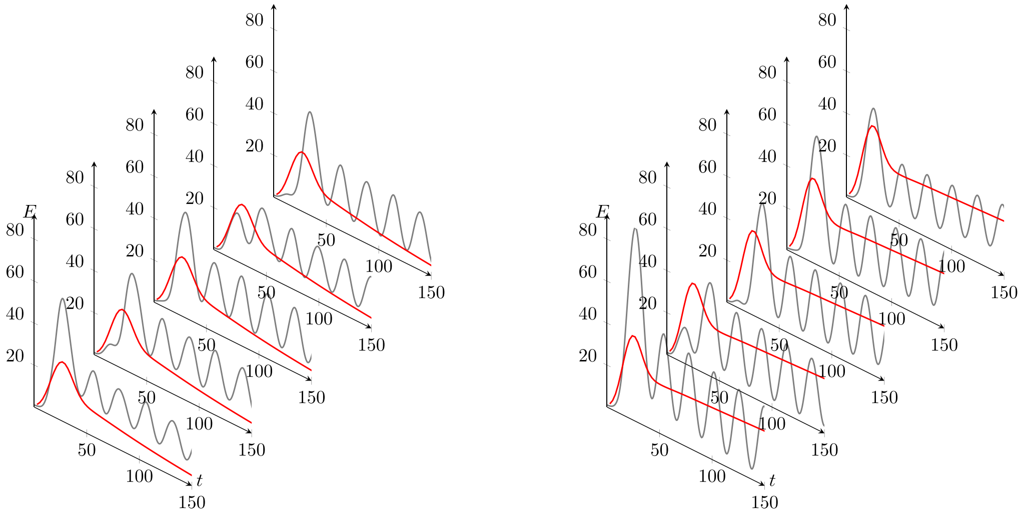

(a) $\alpha = 0.8$

(b) $\alpha = 1$

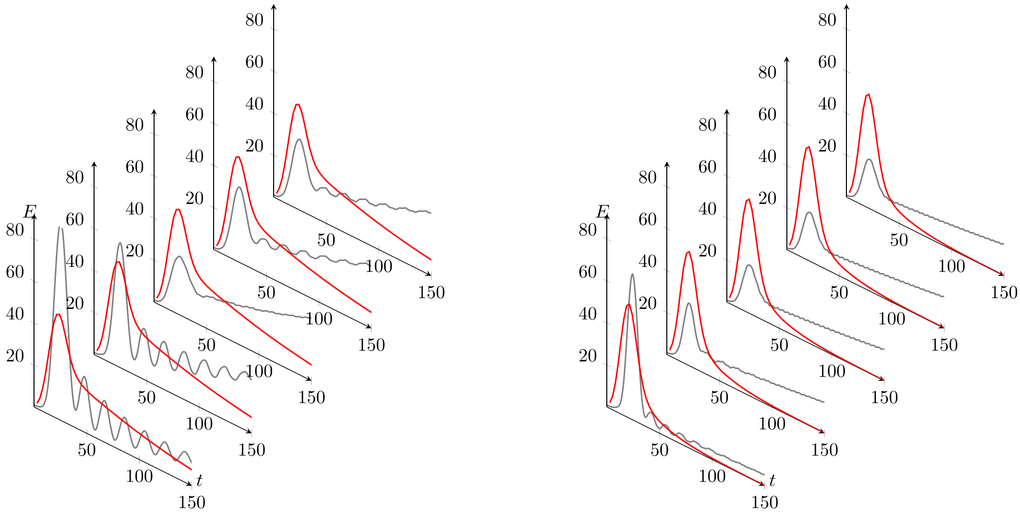

(c) $\alpha = 1.2$

(d) $\alpha = 1.4$

FIG. 9. Time evolution of the total energy for the optimal initial perturbation for $\tau = 26$, 66, 133, 200, 266 (from the left to the right) and $\alpha = 0.8$, 1, 1.2, 1.4. The Reynolds number is fixed to $\mathrm{Re} = 8300$ and the reduced velocity is set to $V_R = 0.7$. In red, the envelope G for the rigid case is represented.

with a damping rate close to the TS mode. When considering the subspace where the TS mode is removed, the total energy peak damping is quite important, which indicates the strong influence of the TS mode in the dynamics. For $V_R = 0.7$, the dynamics is modified. For this value of reduced velocity and chosen parameters, the TWF mode is temporally amplified for long times, while the TS mode is damped temporally. It is consistent with the time evolution of $E(t)$ for the subsets of modes excluding either the TS mode or the TWF mode. It has as a consequence that the oscillations observed for the full system are not driven anymore by the temporal amplification rate of the TS wave. One may also note that while the dynamics for the subspace excluding the TS mode exhibits an exponential growth for $t > 50$, the inclusion of the TS mode leads to a delay of the onset of the

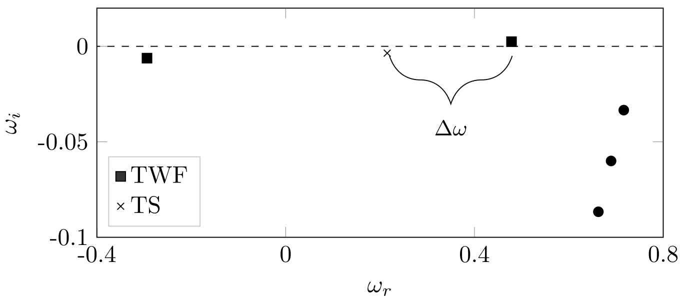

FIG. 10. Spectrum for Re $= 8300$, $V_R = 0.7$, and $\alpha = 1$.

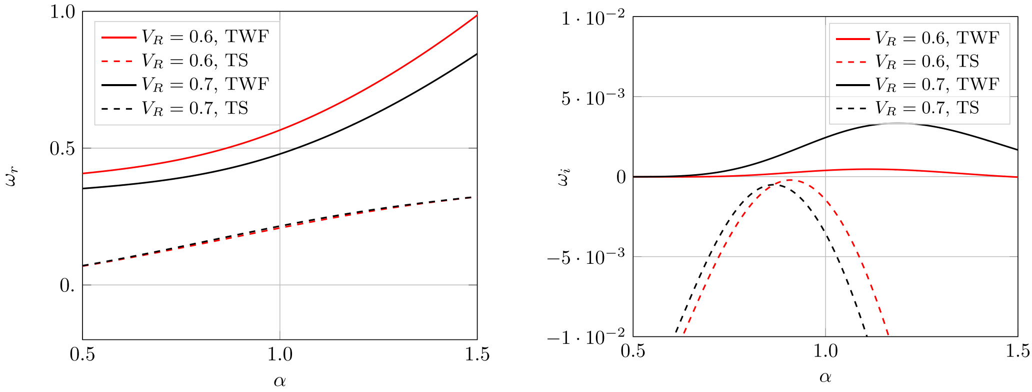

(a) (b)

FIG. 11. (a) Circular frequency ω_r versus the streamwise wavenumber α and (b) temporal amplification rate ω_i versus α for TS and TWF modes and Re $= 8300$, $V_R = 0.7$.

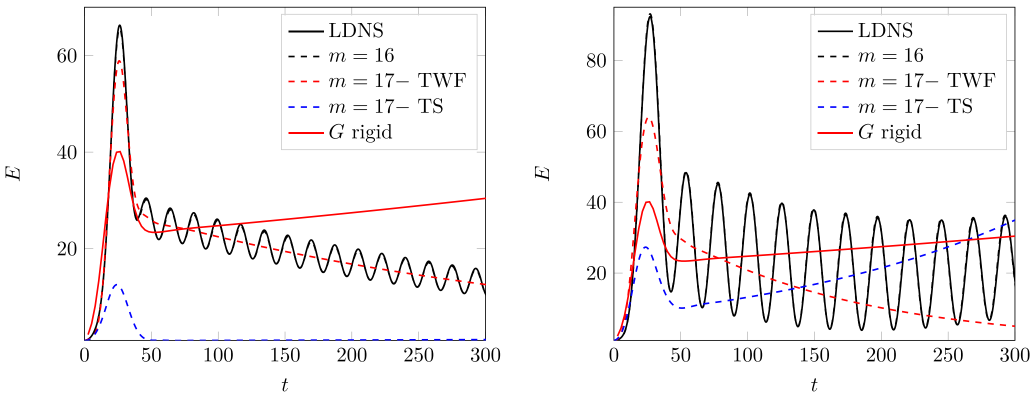

(a) $V_R = 0.6$ (b) $V_R = 0.7$

FIG. 12. Total energy evolution for the optimal initial perturbation projected onto different subsets of eigenmodes for Re $= 8300$, $\alpha = 1$, $\tau = 26$, and $V_R = 0.6$, 0.7. The envelope G for the rigid case is also reported.

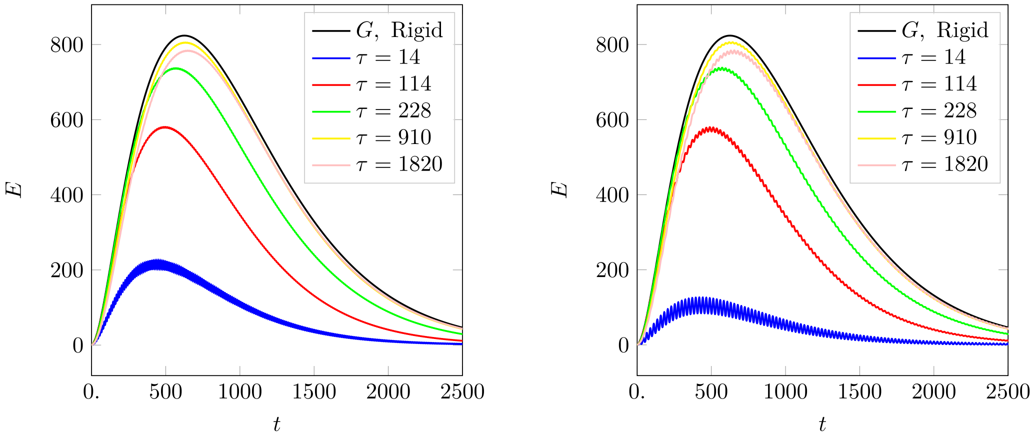

(a) $V_R = 0.4$ (b) $V_R = 0.8$

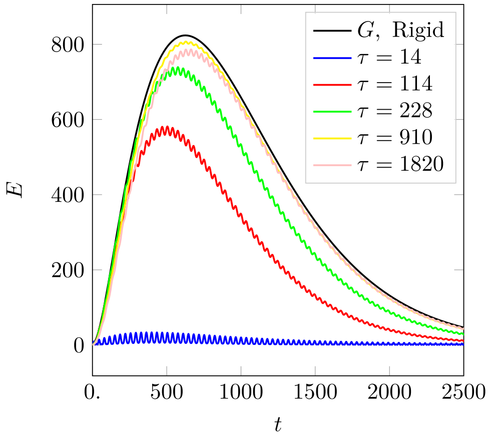

(c) $V_R = 1.2$

FIG. 13. Time evolution of the total energy for Re $= 6666$, $\beta = 0.5$, and $V_R = 0.4$, 0.8, and 1.2 and sinuous initial optimal perturbations computed for τ varying from 14 to 1820. The envelope G for the rigid case is also reported.

total energy growth of the TWF mode. Finally, Fig. 12 shows that an increase of the wall compliance enhances the total energy peak for short times and amplifies the amplitude of the oscillations.

B. Optimal growth for $\alpha = 0$

In this section, we focus on the behavior of perturbations which are infinitely elongated in the streamwise direction x. The transient energy developments are shown in Figs. 13 and 14 for $\beta = 0.5$ and Re $= 6666$ for the sinuous and varicose symmetries, respectively. The reduced velocity ranges from $V_R = 0.4$ to $V_R = 1.2$ and the target time is varying from $\tau = 14$ to $\tau = 1820$. For comparison purposes, the envelope G is also represented for the rigid-wall case only. For all V_R that are considered, the energy curves exhibit a lower growth than the rigid-wall case and their time evolution features fast oscillations for both symmetries. As discussed in Refs. [17,18], the frequency beating correlates with the frequency of the TWF eigenmodes. As also observed for the two-dimensional (2D) case, the transient energy growth exhibits a larger amplification for the

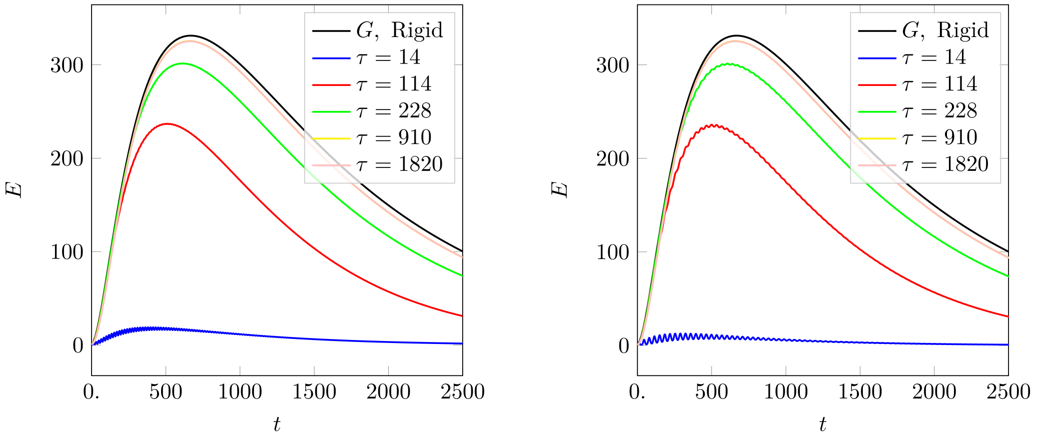

(a) $V_R = 0.4$

(b) $V_R = 0.8$

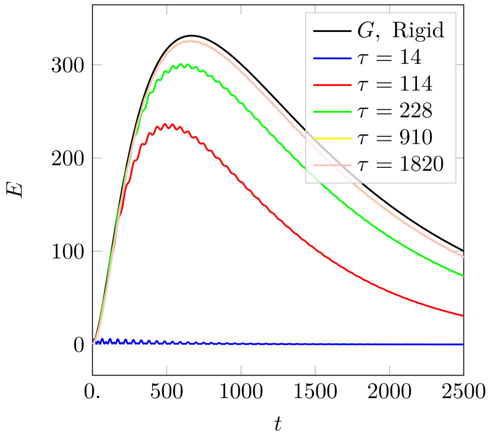

(c) $V_R = 1.2$

FIG. 14. Time evolution of the total energy for $\mathrm{Re} = 6666$, $\beta = 0.5$, and $V_R = 0.4$, 0.8, and 1.2 and varicose initial optimal perturbations computed for τ varying from 14 to 1820. The envelope G for the rigid case is also reported.

sinuous symmetry than the varicose one. For this reason, we restrict our analysis to the sinuous configuration hereafter.

For illustration purposes, we show in Fig. 15(a) the spectrum for the same flow case and $V_R = 1.2$. The figure shows that, in addition to the rigid flow case, there are two eigenmodes that arise from the fluid-structure interaction as observed in the previous section for $\beta = 0$, i.e., two TWF modes propagating in opposite directions. The absolute value of their corresponding circular frequency is noted ω_{TWF} below. For very large V_R, Hœpffner *et al.* [17] (see discussion in section 5.2) have shown that the transient growth is mainly due to the interaction between the two TWF modes where their superposition generates a standing wave that exhibits a low-frequency process. The latter is characterized by a beating period equal to $2\pi/\omega_{\mathrm{TWF}}$.

In Fig. 15(b), the total energy time development associated with the initial optimal perturbation obtained for $\tau = 14$ is reported. For a purely standing wave, the regular pattern is oscillating up and down; as a consequence the beating period associated with its total energy corresponds to $\pi/\omega_{\mathrm{TWF}}$.

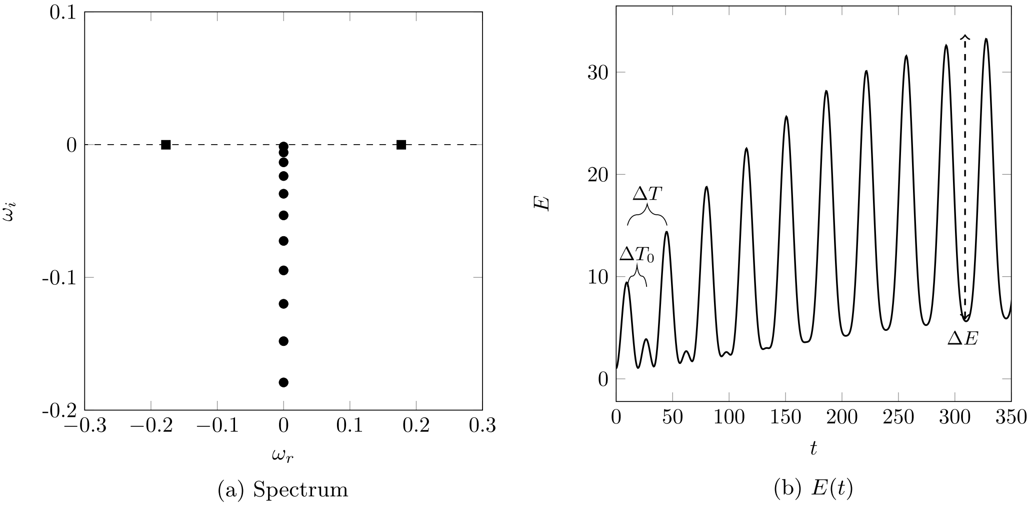

(a) Spectrum

(b) $E(t)$

FIG. 15. (a) Spectrum at $\beta = 0.5$, $V_R = 1.2$, and Re = 6666. (b) Time evolution of the total energy growth for the initial optimal perturbation computed for $\tau = 14$.

For short times, this is precisely what is observed in Fig. 15(b) (noted ΔT_0). As the perturbation evolves in time, its total energy exhibits a characteristic oscillation of period $\Delta T = 2\pi/\omega_{\mathrm{TWF}}$. It seems to indicate that, for these values of V_R, the mechanism is more complex than a simple superposition of the two TWF modes.

To further investigate the origin of the beating and the impact of the TWF modes on the transient energy growth, we project the initial perturbation on a subspace spanned by a reduced number of eigenmodes, as in the previous section. In Fig. 16(a), $E(t)$ is shown for both the complete LDNS and the reduced-order model (ROM) based on 50 eigenmodes for validation purposes. One may observe a perfect agreement between the two simulations. In the figure, the time evolution of the total energy is also represented for a subset including only the two TWF modes. It generates a standing wave with a characteristic frequency ω_{TWF}. However, its growth in time is far from matching the one given by the LDNS.

In Fig. 16(b), $E(t)$ is plotted for $m = 50$ excluding the TWF modes. The total energy evolution for the rigid-wall case is also reported. This total energy curve does not show any beating process and it displays a transient amplification comparable to the situation prevailing for rigid walls (i.e., associated with a pair of streamwise vortices which generates streaks). In particular, the growth for large times is much higher than the one including TWF modes. It indicates that the inclusion of TWF modes yields to destructive interferences that tend to damp the transient energy growth associated with streak amplification.

Let us now consider an initial perturbation resulting from the superposition of the two previous subsets of modes (i.e., the standing wave and the pair of streamwise vortices). The time evolution of its total energy is shown in Fig. 17. The figure shows that the curve almost matches the one associated with the optimal initial perturbation. It shows that the subsets of modes associated with TWF modes and the discrete branch are nearly orthogonal. Hence, the mechanism seems to be linked to a standing wave oscillating in a streaky developing flow.

The modification of the transient growth mechanism due to the TWF modes is also illustrated through cross sections of velocity components extracted at various times in Figs. 18–20.

In Fig. 18, the time evolution of the optimal perturbation obtained by LDNS is represented for a time interval equal to ΔT. The figure shows that TWF modes lead to damping the intensity of the pair of streamwise vortices during one cycle of the standing wave. It has as a consequence to annihilate the generation of streaks which is consistent with results given in Fig. 16.

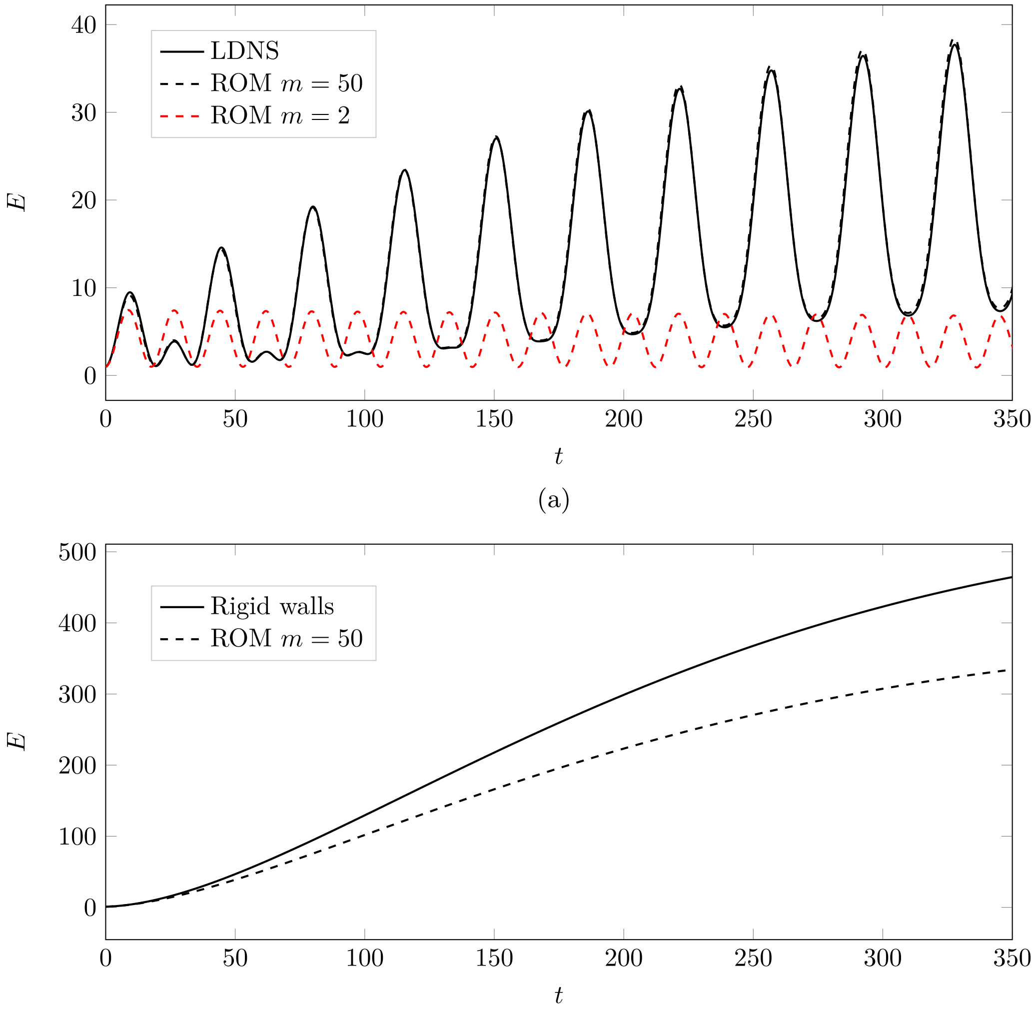

(a)

(b)

FIG. 16. Time evolutions for the total energy growth for $\beta = 0.5$, $V_R = 1.2$, $\mathrm{Re} = 6666$, and $\tau = 14$. (a) LDNS are compared with ROMs for $m = 50$ eigenmodes and the two TWF modes (referenced as $m = 2$). (b) Total energy curves computed with the ROM for $m = 50$ excluding the TWF modes are compared to the rigid-wall case.

A similar simulation is shown in Fig. 19, where the optimal initial perturbation is projected onto the two TWF modes. A purely standing-wave behavior is observed, where the perturbation is mainly concentrated near the walls and oscillates around zero. Finally, the last configuration where the TWF modes are removed from the subset of modes is depicted in Fig. 20. The evolution of the initial perturbation exhibits the fundamental bricks of the lift-up effect, i.e., a pair of streamwise vortices that generate low- and high-speed streaks.

Then, for this value of V_R where the coupling between the fluid and compliant walls is more effective, the importance of the interactions between TWF modes and the discrete branch is crucial to fully describe the phenomenon instead of what is observed for very large values of V_R when the system is governed only by the standing wave (i.e., mainly an effect of the walls [17]).

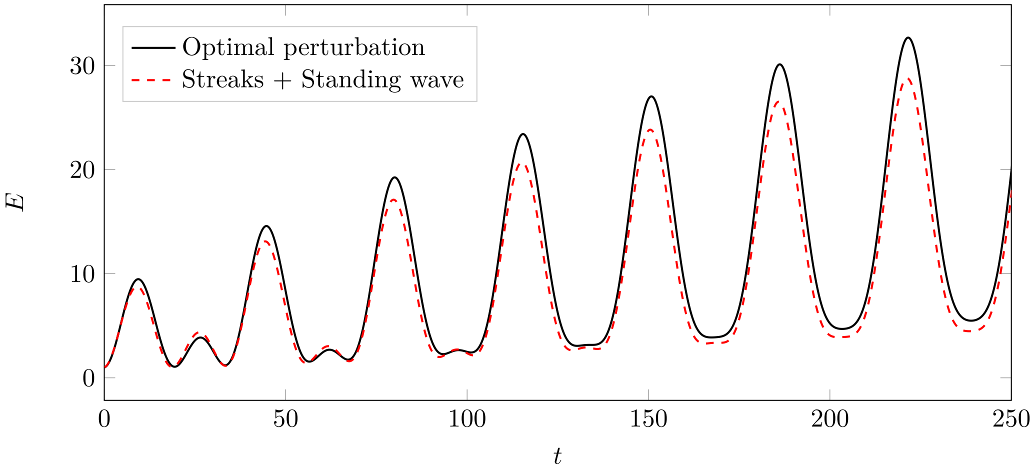

FIG. 17. Time evolutions for the total energy growth for $\beta = 0.5$, $V_R = 1.2$, Re = 6666, and $\tau = 14$. The evolution of $E(t)$ for the initial perturbation restricted to the summation of the pair of streamwise vortices and the standing waves is compared to $E(t)$ associated with the optimal perturbation.

Let us now characterize the influence of some parameters on these oscillations. We introduce the quantity $\Delta E(\tau, \text{Re}, V_R, \beta)$ which measures the amplitude of the oscillations [see Fig. 15(b)]. In particular, we consider hereafter, $\Delta E^M(\text{Re}, V_R, \beta) = \max_\tau \Delta E(\tau, \text{Re}, V_R, \beta)$. The distribution of

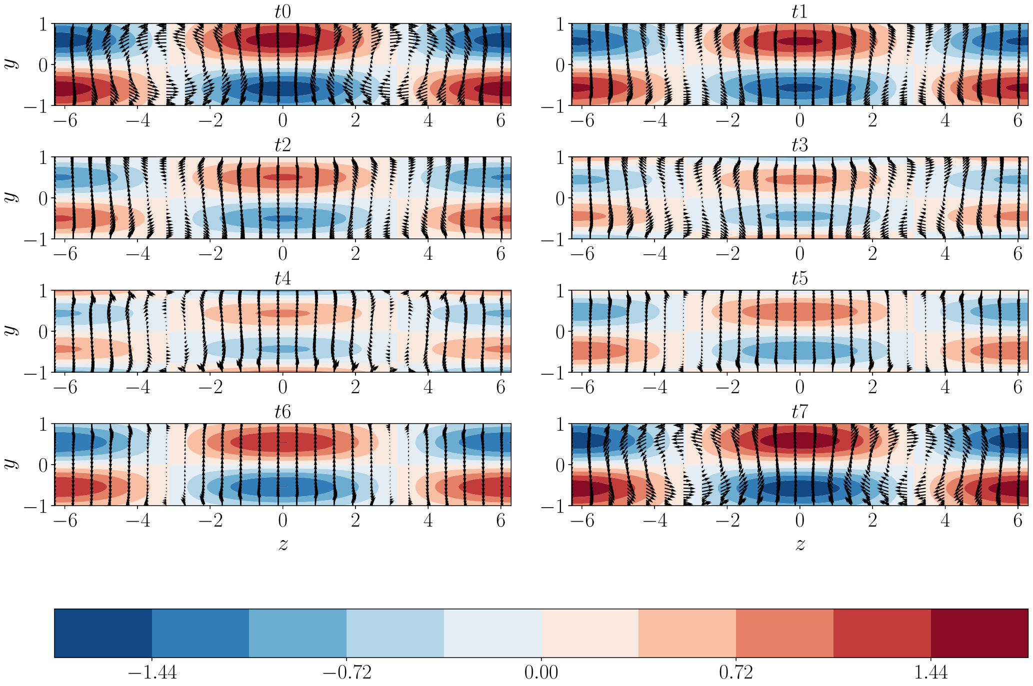

FIG. 18. Cross sections of the optimal perturbation for $\beta = 0.5$, Re = 6666, $V_r = 1.2$, and $\tau = 14$ in the (z, y) plane for $tk = t_i + k/8\Delta T$ with k varying from 0 to 7 and $t_i = 8.7$. Vectors for the cross-stream components and isocontours of the streamwise velocity fields are shown.

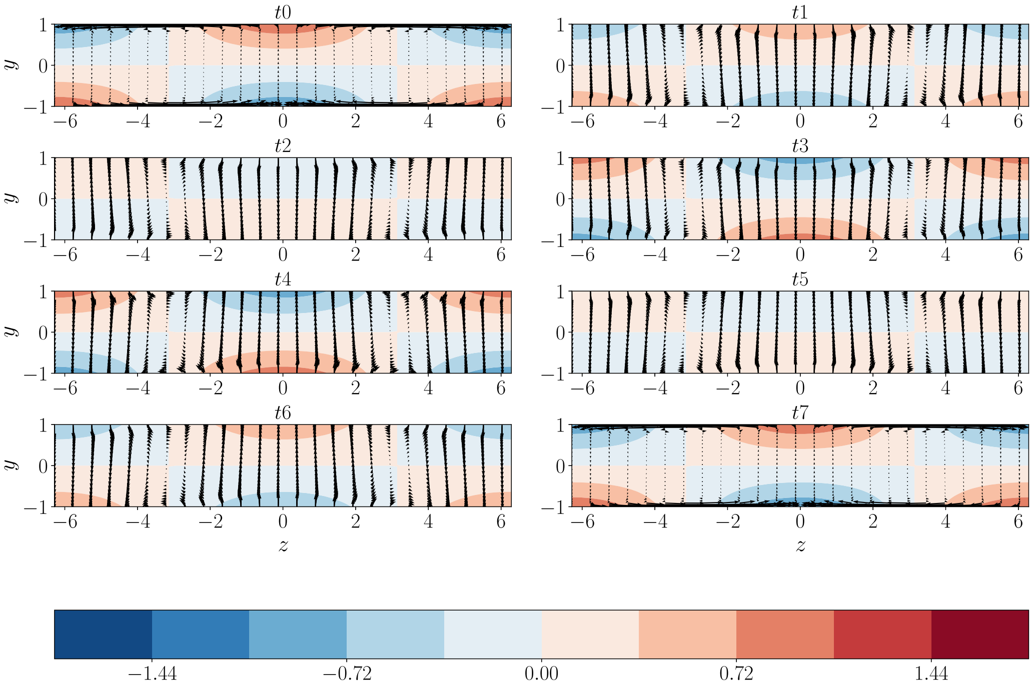

FIG. 19. Cross sections of the optimal perturbation projected onto the two TWF modes for $\beta = 0.5$, $\mathrm{Re} = 6666$, $V_r = 1.2$, and $\tau = 14$ in the (z, y) plane for $tk = t_i + k/8\Delta T$ with k varying from 0 to 7 and $t_i = 8.7$. Vectors for the cross-stream components and isocontours of the streamwise velocity fields are shown.

ΔE^M as a function of V_R and β for Re = 6666 is shown in Fig. 21. The figure shows that $\Delta E^M(V_R)$ exhibits an almost linear behavior for all spanwise wavenumbers that are investigated. The behavior of the amplitude of the standing-wave oscillation is then further outlined with the parameter A obtained by using the linear approximation $\Delta E^M(\mathrm{Re}, V_R, \beta) \approx A(\mathrm{Re}, \beta)V_R$. The distribution of A with β for three Reynolds numbers is shown in Fig. 21(b). The figure shows that A peaks for spanwise wavenumbers much smaller than the optimal value of β for streaks and rigid walls (i.e., $\beta = 2$). Besides, the amplitude of the oscillations increases with the Reynolds number and the peak in A is reached for a spanwise wavenumber around $\beta \approx 0.7 - 0.8$ independently of Re. It may confirm the strong interplay between the streaks and the standing wave to dictate the amplitude of the oscillations for this range of V_R, since the TWF modes are mainly independent of the Reynolds number [15].

As discussed above, the frequency of the standing wave is associated with the circular frequency of the TWF mode. In Fig. 22, the distribution of the circular frequency of the TWF mode is shown as a function of V_R and β. Some computations at various Reynolds numbers confirmed that the circular frequency is not dependent on Re (not shown here). The figure shows that the standing-wave frequency is decreasing with an increase of V_R and a decrease in β. In the figure, we also report the added-mass model derived by Hœpffner *et al.* [17]. In this model, the authors approximate the wall-normal flow velocity profiles with an exponential curve. Hence, by using an integration along the wall-normal direction of the momentum equation, the action of the pressure force can be associated with an added-mass effect. The equation of the circular frequency is then

$$\omega^2 = \frac{1}{m + m_a}(B\beta^4 + K),$$

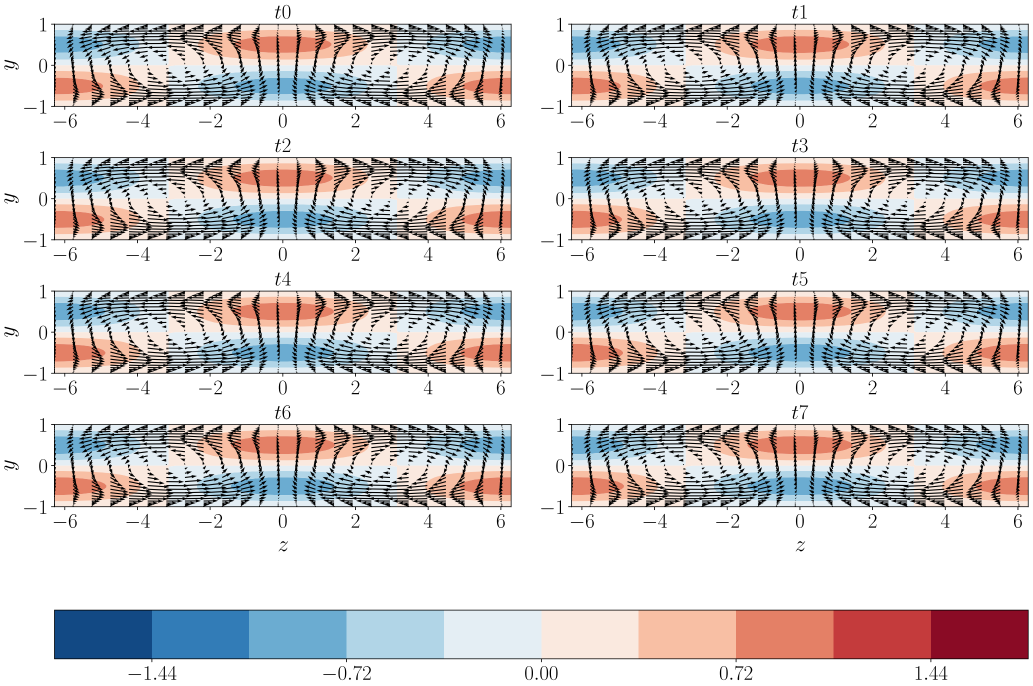

FIG. 20. Cross sections of the optimal perturbation projected onto 50 eigenmodes excluding the two TWF modes for $\beta = 0.5$, Re $= 6666$, $V_r = 1.2$, and $\tau = 14$ in the (z, y) plane for $tk = t_i + k/8\Delta T$ with k varying from 0 to 7 and $t_i = 256$. Vectors for the cross-stream components and isocontours of the streamwise velocity fields are shown.

with $m_a = \rho h(1 - e^{-\beta})/\beta$. The corresponding values are reported as dashed lines in Fig. 22 where an almost perfect match is observed with the full computation. It validates this model also for moderate values of the reduced velocity.

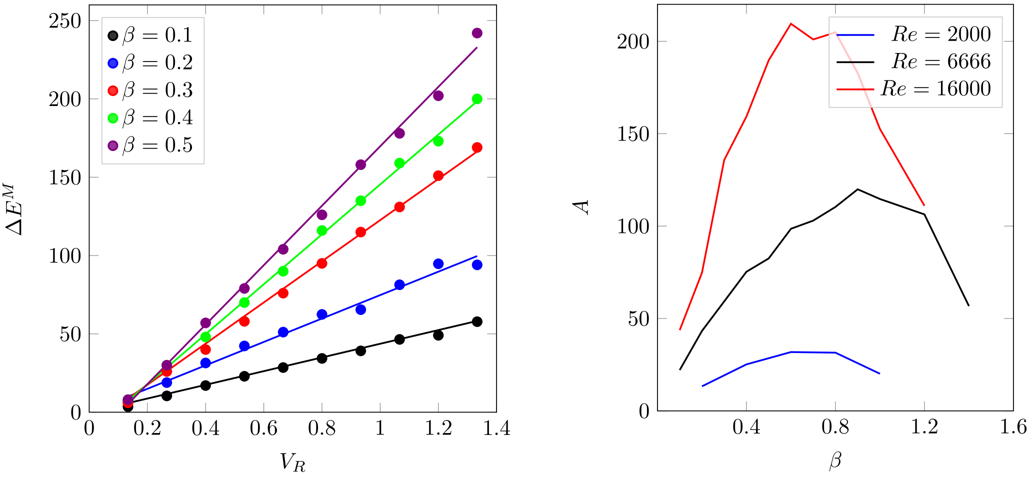

(a)

(b)

FIG. 21. Amplitude of the oscillations. (a) Distribution of ΔE^M with V_R for various β and Re $= 16000$. (b) Distribution of A as a function of β for Re $= 2000$, 6666, and 16 000.

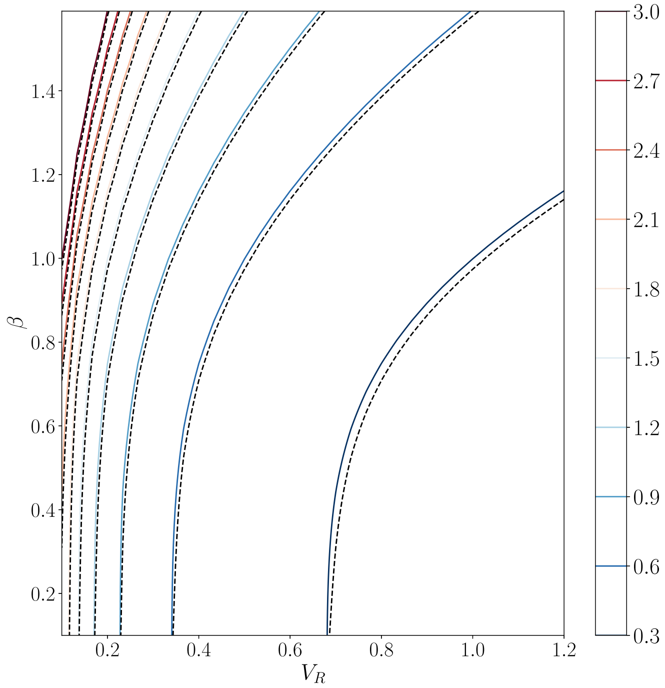

FIG. 22. Frequency of the standing wave as a function of β and V_R. Dashed lines denote the frequency computed with the added-mass model.

VII. DISCUSSION AND CONCLUSIONS

In this paper, the temporal nonmodal growth of two- and three-dimensional perturbations in channel flow over infinite compliant walls has been investigated. From the formalism point of view, we have developed a Lagrangian framework for the constrained optimization problem associated with the linearized fluid-structure interaction system. In comparison with methods used by Hœpffner *et al.* [17] and Zengl and Rist [18] for the same case, which are based on the summation of eigenmodes, the present technique is free of numerical spurious oscillations. The short-time dynamics for either the 2D case or infinitely elongated structures in the streamwise direction is mostly amplified for the sinuous configuration. As a consequence, a large part of the study concerns the sinuous symmetry of the system.

Besides this point, the two key findings from this work are the following. First, for a perturbation developing in the streamwise–wall-normal plane, the short-time dynamics is seen to be strongly modified by the flexibility of the wall. More specifically, a close inspection of the projection of the dynamics onto a subset of modes shows that the coupling between the TS and TWF modes generates strong oscillations. For some range of parameters, when the frequencies of TS and TWF modes are similar, the amplitude of the modulation reaches higher levels than the optimal gain associated with the rigid-wall case. Hence, while the wall compliance contributes to reduce the amplification of TS modes, the total energy growth for short times is enhanced, however. We hope that the present study clearly shows the important roles, in the short-time dynamics, of TS and TWF modes as well as some of the other branches of discrete modes, and could therefore be useful to design a simplified model describing the full dynamics as has been done for the asymptotic regime by Davies and Carpenter [13].

Second, it has been found that the transient dynamics for streamwise-invariant perturbations and $\mathcal{O}(1)$ values of the reduced velocity V_R is driven by the superposition of a standing wave (due to the interaction between two oppositely propagating TWF modes) and the roll-streak dynamics. In particular, the two corresponding subsets appear nearly orthogonal to each other. The dynamics of the standing wave was clearly highlighted by Hœpffner *et al.* [17]. However, the case studied by these authors was associated with a very high value of the reduced velocity ($V_R \approx 23.5$) and for this specific case, the roll-streak dynamics was totally overwhelmed by the large temporal oscillations of the standing wave. In particular, as underlined in a recent study by Lebbal *et al.* [22], typical values of V_R for blood flow rate and arterial diameters are in the range 0.1–0.2. For aerodynamics applications, the boundary-layer flow interacting with a Kramer-type compliant wall detailed by Wiplier and Ehrenstein [11] gives a reduced velocity of approximately $V_R = 0.4$. Hence, the value used in Ref. [17] is clearly out of range of these applications.

Finally, we provide scaling laws for the amplitude of the oscillations with the Reynolds number, spanwise wave numbers, and critical reduced velocity. The variation of its characteristic frequency is also investigated. For this last point, the added-mass model derived by Hœpffner *et al.* [17] is seen to describe perfectly well the period of the oscillations but not the amplitude of the standing-wave oscillation. As discussed above, the case considered by Hœpffner *et al.* [17] is only associated with large V_R where the dynamics of the full system is mainly driven by the traveling-wave flutter modes. However, as it is shown in the present study, for moderate values of V_R, where there is a stronger interaction between streaks and the standing wave, the model fails to reproduce the full dynamics because it does not include the time evolution of streaks.

Using a range of computations, we show that the amplitude of the oscillation increases linearly with the reduced velocity V_R for a given spanwise wavenumber and Reynolds number. In addition, the optimal spanwise wavenumber leading to the maximum wave oscillation is around $\beta = 0.7$ which can be compared with $\beta = 2$ associated with the spanwise scale that maximizes the streaks amplification. In particular, for β around 0.7, the amplification of streaks is seen to be damped by the standing-wave dynamics. We then hope that these results could be a first step to extend the model derived by Hœpffner *et al.* [17] to moderate values of V_R.

The study could now be adapted without any numerical complications to time-periodic flows which are more representative of artery blood flow, in the same fashion as Pier and Schmid [29] have recently done for the rigid-wall case. The extension of the present analysis to the pipe flow case is also under current intensive scrutiny.

ACKNOWLEDGMENT

Fédération Lyonnaise de Modélisation et Sciences Numériques (FLMSN) is gratefully acknowledged for providing access to high-performance computing resources.

[1] M. Kramer, Boundary layer stabilization by distributed damping, J. Aerosp. Sci. **27**, 69 (1960).

[2] M. Gad-el-Hak, Boundary layer interactions with compliant coatings: An overview, Appl. Mech. Rev. **39**, 511 (1986).

[3] P. T. Nagy, A. Szabó, and G. Paál, The effect of spanwise and streamwise elastic coating on boundary layer transition, J. Fluids Struct. **110**, 103521 (2022).

[4] J. B. Grotberg and O. E. Jensen, Biofluid mechanics in flexible tubes, Annu. Rev. Fluid Mech. **36**, 121 (2004).

[5] P. G. Larose and J. B. Grotberg, Flutter and long-wave instabilities in compliant channels conveying developing flows, J. Fluid Mech. **331**, 37 (1997).

[6] V. Kumaran, Stability and the transition to turbulence in the flow through conduits with compliant walls, J. Fluid Mech. **924**, P1 (2021).

[7] P. W. Carpenter and A. D. Garrad, The hydrodynamic stability of flow over Kramer-type compliant surfaces. Part 1. Tollmien-Schlichting instabilities, J. Fluid Mech. **155**, 465 (1985).

[8] P. W. Carpenter and A. D. Garrad, The hydrodynamic stability of flow over Kramer-type compliant surfaces. Part 2. Flow-induced surface instabilities, J. Fluid Mech. **170**, 199 (1986).

[9] J. W. Miles, On the generation of surface waves by shear flows, J. Fluid Mech. **3**, 185 (1957).

[10] T. B. Benjamin, Shearing flow over a wavy boundary, J. Fluid Mech. **6**, 161 (1959).

[11] O. Wiplier and U. Ehrenstein, Numerical simulation of linear and nonlinear disturbance evolution in a boundary layer with compliant walls, J. Fluids Struct. **14**, 157 (2000).

[12] M. Malik, M. Skote, and R. Bouffanais, Growth mechanisms of perturbations in boundary layers over a compliant wall, Phys. Rev. Fluids **3**, 013903 (2018).

[13] C. Davies and P. W. Carpenter, Instabilities in a plane channel flow between compliant walls, J. Fluid Mech. **352**, 205 (1997).

[14] V. Shankar and V. Kumaran, Stability of wall modes in fluid flow past a flexible surface, Phys. Fluids **14**, 2324 (2002).

[15] S. Lebbal, F. Alizard, and B. Pier, Revisiting the linear instabilities of plane channel flow between compliant walls, Phys. Rev. Fluids **7**, 023903 (2022).

[16] D. Wang, X. Luo, Z. Liu, and P. S. Stewart, Flow-induced surface instabilities in a flexible-walled channel with a heavy wall, J. Fluid Mech. **956**, A1 (2023).

[17] J. Hœpffner, A. Bottaro, and J. Favier, Mechanisms of non-modal energy amplification in channel flow between compliant walls, J. Fluid Mech. **642**, 489 (2010).

[18] M. Zengl and U. Rist, Linear-stability investigations for flow-control experiments related to flow over compliant walls, in *Nature-Inspired Fluid Mechanics*, Notes on Numerical Fluid Mechanics and Multidisciplinary Design Vol. 119 (Springer, Berlin, 2012), pp. 223–237.

[19] K. Tsigklifis and A. D. Lucey, Asymptotic stability and transient growth in pulsatile Poiseuille flow through a compliant channel, J. Fluid Mech. **820**, 370 (2017).

[20] E. de Langre, Analyse dimensionnelle en interaction fluide–structure, Houille Blanche **86**, 14 (2000).

[21] C. Davies and P. W. Carpenter, Numerical simulation of the evolution of Tollmien-Schlichting waves over finite compliant panels, J. Fluid Mech. **335**, 361 (1997).

[22] S. Lebbal, F. Alizard, and B. Pier, Linear instabilities of pulsatile plane channel flow between compliant walls, J. Fluid Mech. **948**, A15 (2022).

[23] P. J. Schmid and D. S. Henningson, *Stability and Transition in Shear Flows*, Applied Mathematical Sciences Vol. 142 (Springer, Berlin, 2001).

[24] F. Alizard, L. Le Penven, A. Cadiou, B. Di Pierro, and M. Buffat, Restricted optimal paths to transition in a plane Couette flow, Eur. J. Mech. B: Fluids **85**, 261 (2021).

[25] R. Peyret, *Spectral Methods for Incompressible Viscous Flow* (Springer, New York, 2002).

[26] L. Trefethen, *Spectral Methods in Matlab* (SIAM, Philadelphia, 2000).

[27] F. Alizard and D. Biau, Restricted nonlinear model for high- and low-drag events in plane channel flow, J. Fluid Mech. **864**, 221 (2019).

[28] F. Alizard and J. C. Robinet, Modeling of optimal perturbations in flat plate boundary layer using global modes: Benefits and limits, Theor. Comput. Fluid Dyn. **25**, 147 (2011).

[29] B. Pier and P. J. Schmid, Optimal energy growth in pulsatile channel and pipe flows, J. Fluid Mech. **926**, A11 (2021).